Progress in Nuclear Energy 180 (2025) 105636

Contents lists available at ScienceDirect

Progress in Nuclear Energy

journal homepage: www.elsevier.com/locate/pnucene

Seismic performance of AP1000 nuclear power plants in earthquake-prone regions: A case study of the 2023 Türkiye earthquakes

Tandogan Mesut [a], Duy-Duan Nguyen [b], Duy-Liem Nguyen [c], Duc-Kien Thai [a,*]

[a] Department of Civil and Environmental Engineering, Sejong University, 209 Neungdong-ro, Gwangjin-gu, Seoul, 05006, Republic of Korea
[b] Department of Civil Engineering, Vinh University, Vinh, 461010, Viet Nam
[c] Department of Civil Engineering and Applied Mechanics, Ho Chi Minh City University of Technology and Education, 1 Vo Van Ngan St., Thu Duc District, Ho Chi Minh City, Viet Nam

A R T I C L E I N F O

Keywords:
AP1000 nuclear power plant
Seismic performance
Numerical modeling and simulation
Mainshock-aftershock sequence
The 2023 Türkiye earthquake

A B S T R A C T

Safety assessment of nuclear power plants (NPPs) is crucial, especially considering the influence of earthquakes. This study evaluates the structural performance and damage analysis of the AP1000 NPP subjected to the recent severe earthquakes in Türkiye in 2023. Numerical modeling and simulations were developed in ABAQUS to evaluate the structural responses, plastic damage characteristics, strain states, and energy dissipation of the reinforced concrete shield building (RCSB). To ensure a robust evaluation, three artificial earthquakes, based on the Regulatory Guide (RG) 1.60 spectrum, were used as benchmark scenarios representing Operating Basis Earthquake (OBE), Safe Shutdown Earthquake (SSE), and Safe Shutdown Margin Earthquake (SME) levels. Twelve ground motion records in various stations during the 2023 Türkiye earthquakes were selected for nonlinear time-history analyses. The results revealed a significant variability in structural performance across different locations affected by those earthquakes. The RCSB structure generally exhibited a tension failure under sequential earthquakes. Among 12 investigated records, the structure subjected to ones at the Pazarcık station and Hatay province stations showed significant damage. While maximum principal strain and tension damage parameters of RCSB exceeded allowable levels under records with high peak ground acceleration, only the case using the Pazarcık record showed a significant compressive damage. Moreover, it is recommended that NPP construction should be avoided in particularly vulnerable areas like Hatay and Kahramanmaraş provinces, where structural responses exceeded the SSE level. In contrast, records from Adana and Mersin provinces showed insignificant effects from the earthquakes, indicating a need for further study using different earthquake records recorded in those areas. This study also highlighted the importance of considering the effect of mainshock-aftershock sequences on the seismic performance evaluation of NPP structures.

Nomenclature

0119, 0120 …	Station codes
AE	Artificial earthquake
C0119, C0120 …	Combined earthquake records from respective stations
DSE	Design Safe Earthquake
EPRI NP	Electric Power Research Institute
FEA	Finite element analysis
FEM	Finite element model
IAEA	International Atomic Energy Agency
KINS	Korea Institute of Nuclear Safety
LS	Limit State
MRD	Maximum relative displacements

(*continued on next column*)

(*continued*)

0119, 0120 …	Station codes
NRC	U.S. Nuclear Regulatory Commission
NPP	Nuclear power plant
NUREG	Nuclear Regulatory Commission
OBE	Operating Basis Earthquake
PAMF	Peak acceleration magnification factor
PFA	Peak floor accelerations
PGA	Peak ground acceleration
RCC	Reinforced concrete containment
RCSB	Reinforced concrete shield building
RG	Regulatory Guide
RLE	Review Level Earthquake

(*continued on next page*)

* Corresponding author.
E-mail address: thaiduckien@sejong.ac.kr (D.-K. Thai).

https://doi.org/10.1016/j.pnucene.2025.105636
Received 13 August 2024; Received in revised form 10 January 2025; Accepted 21 January 2025
Available online 30 January 2025

(*continued*)

0119, 0120 …	Station codes
SSC	Structures, systems, and component
SSE	Safe Shutdown Earthquake
SME	Safe Shutdown Margin Earthquake
TADAS	Turkish Accelerometric Database and Analysis System
α	decay parameter of equation of concrete
α and β	Rayleigh damping coefficients
$\mathbf{C}$	damping matrix
D_e/C	demand-to-capacity ratio
d_c	Compression damage factor
d_t	Tension damage factor
E_c	Elastic modulus of concrete
E_s	Elastic modulus of steel
ε_1	First principal strain
ε_3	Third principal strain
ε_c	Compressive strain of concrete
ε_{c1}	Compressive strain at the ultimate stress of concrete
ε_{cu}	Ultimate compressive strain of concrete
ε_t	Tensile strain of concrete
ε_{tu}	Ultimate tensile strain of concrete
ε_s	Strain of steel
ε_{sy}	Elastic strain of steel
ε_{su}	Ultimate strain of steel
ε_{0c}^{el}	Elastic strain at ultimate elastic compressive stress of concrete
$\tilde{\varepsilon}_c^{in}$	Compressive inelastic strain
$\tilde{\varepsilon}_c^{pl}$	Compressive plastic strain
ε_c^{el}	Compressive elastic strain
ε_{0t}^{el}	Elastic strain at ultimate tensile stress of concrete
$\tilde{\varepsilon}_t^{ck}$	Tensile cracking strain of concrete
$\tilde{\varepsilon}_t^{pl}$	Tensile plastic strain of concrete
ε_t^{el}	Tensile elastic strain of concrete
f_c	Compressive strength of concrete
f_t	Tensile strength of concrete
f_{sy}	Yield strain of steel
$\mathbf{K}$	Stiffness matrix
k	Coefficient of Yin's stress-strain equation of concrete
$\mathbf{M}$	Mass matrix
m	Coefficient of Yin's stress-strain equation of concrete
n	The ratio of the elastic modulus of steel and concrete
R_{epi}	Epicentral distance (radius) between earthquake and station
σ_c	Compressive stress of concrete
σ_t	Tensile stress of concrete
σ_s	Stress of steel
σ_{0c}	Ultimate elastic compressive stress
ρ	Reinforcement ratio
ρ_c	Mass density of concrete
ρ_s	Mass density of steel
υ_c	Poisson's ratio of concrete
υ_s	Poisson's ratio of steel
u	Displacement
$\dot{\mathbf{u}}$	Velocity
$\ddot{u}$	Acceleration
$\ddot{u}_g$	Ground motion acceleration
V_{s30}	Average shear wave velocity in the top 30 m of soil or rock
ζ	Damping ratio
ω_1	Circular frequencies of the first mode
ω_2	Circular frequencies of the second mode

1. Introduction

Nuclear power has emerged as a crucial energy source, addressing the growing global energy demand while maintaining low carbon emissions. Nuclear power plants (NPPs), which generate sustainable energy through controlled nuclear reactions, play an important role in providing electricity production for many countries. In addition to ensuring a stable and abundant supply of water, the seismic safety requirement is also a crucial issue in the design of NPPs, particularly in earthquake-prone regions. Rigorous safety analyses are vital to mitigate the risks posed by seismic activity in nuclear power generation (Xie et al., 2019). These safety assessments involve intricate evaluations of potential seismic hazards and the structural responses of NPPs. Agencies such as the International Atomic Energy Agency (IAEA), the United States Nuclear Regulatory Commission (NRC), and the Korea Institute of Nuclear Safety (KINS) have developed comprehensive methodologies to guide these assessments (Probabilistic Safety Assessment for Seismic, 2020; Methodologies for Seismic Safety Evaluation, 2020; Seismic Hazard Evaluations for, 2021; Seismic Safety and Regulatory Activitie, 2024).

Over the years, numerous studies have evaluated the seismic vulnerability of NPPs worldwide. Traditionally, design codes have focused on assessing the impact of single design earthquakes, ignoring the effects of mainshock-aftershock sequences (Zhai et al., 2015). However, some recent research highlighted the importance of these sequences, which can significantly affect the structural integrity of NPPs (Zhai et al., 2017, 2018; Chen et al., 2021; Wang et al., 2019; Pang et al., 2023a). In civil and structural engineering, researchers have thoroughly examined the inelastic responses of various structures, including steel and reinforced concrete buildings and bridges, subjected to mainshock-aftershock ground motions (Zhang et al., 2013; Hatzigeorgiou and Beskos, 2009; Abdelnaby and Elnashai, 2015; Fakharifar et al., 2015; Cui et al., 2024). For NPPs, considering mainshock-aftershock sequences in the seismic performance evaluation and design process is necessary.

Zhai et al. (2015) studied a reinforced concrete containment (RCC) building of an NPP under ten recorded seismic sequences adapted to 0.3g peak ground acceleration (PGA) with two horizontal components. Their findings demonstrated that aftershocks significantly affect the RCC's responses, including maximum top accelerations, top displacements, and accumulated damage. A follow-up study by the same researchers indicated that the impact of mainshock-aftershock sequences could be neglected in isolated RCC buildings (Zhai et al., 2017). Several studies suggested that aftershocks could increase cumulative damage and influence the seismic performance of NPPs, particularly affecting the floor acceleration response spectrum (Yu et al., 2019; Zhao et al., 2020a; Pang et al., 2023b; Zhang et al., 2024). While aftershocks significantly affected maximum acceleration, peak displacement, acceleration response spectrum, and stress distribution of non-isolated NPP buildings, isolation systems can mitigate these effects (Zhao et al., 2020b). Chen et al. (2021) focused on the seismic damage analysis of the entire AP1000 NPP during strong seismic sequences using seven synthetic mainshock-aftershock excitations. The results showed that concrete damage was greatly developed beyond the design basis earthquake sequence with increasing PGA and aggravated by the aftershock. Specifically, concrete tension damage was more severe than compression damage under earthquake sequences, and structural residual displacement and damage dissipation energy increased due to the aftershocks.

Türkiye has historically been subjected to significant earthquakes. Over the past century, Turkey has experienced several catastrophic earthquakes with magnitudes exceeding Mw 7, including the 1939 Erzincan earthquake, the 1999 Gölcük earthquake, and the 1999 Düzce earthquake. In earthquake-prone countries like Türkiye – which has recently adopted nuclear energy as part of its strategy to meet growing energy demands, with one nuclear power plant currently under construction and plans to increase the number of such facilities in the near future– integrating seismic safety assessments into nuclear energy strategies is crucial. Conducting seismic vulnerability evaluations of NPP structures at potential sites is essential to ensuring safety requirements are met. In 2023, Türkiye experienced significant seismic events, including the Pazarcık, Elbistan, and Yayladağı earthquakes, which contain mainshock-aftershock sequences. This study aims to evaluate the seismic performance of the containment building of AP1000 NPPs subjected to these earthquake events with extremely high PGAs of 2.1g, 0.65g, and 0.85g, respectively. By assessing the seismic vulnerability of various locations, particularly those near water sources, this study examined the effects of these strong earthquakes both individually and sequentially, highlighting the mainshock-aftershock impacts on the structural performances of NPPs. In this study, time history analysis was conducted to apply real earthquake excitations using a method widely

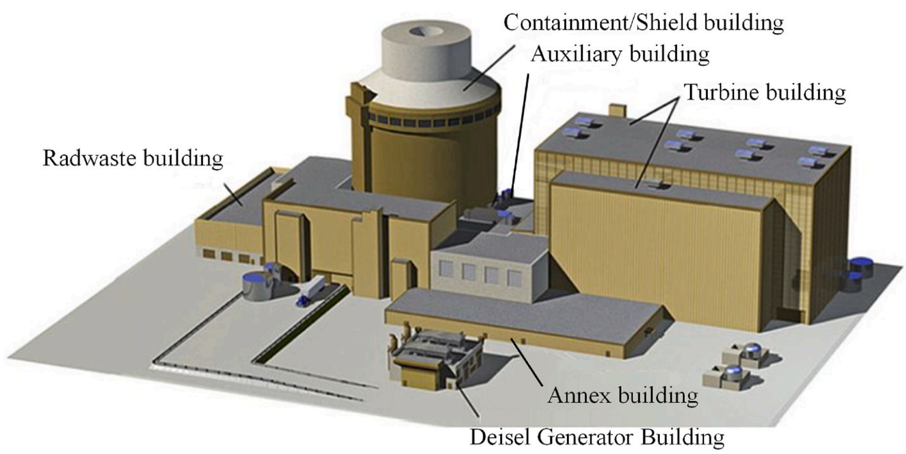

Fig. 1. AP1000 nuclear power plant.

Table 1
Geometric parameters of AP1000 RCSB.

Parameter	Value
Diameter of RCSB	44.200 m
Height of RCSB	81.540 m
Wall thickness of RCSB	0.914 m
Outer diameter of water tank	27.120 m
Inner diameter of water tank	10.600 m
Height of water tank	11.700 m

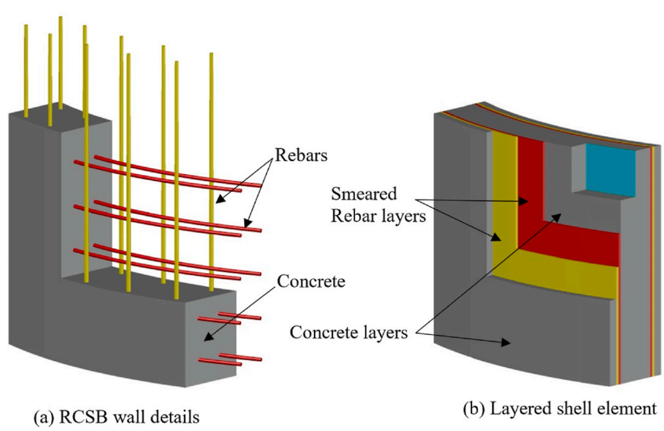

Fig. 2. Layered shell elements.

Table 2
Material properties of AP1000 RCSB.

Material	Parameter	Value
Concrete	Mass density (ρ_c)	2300 kg/m^3
	Elastic modulus (E_c)	26.3 GPa
	Poisson's ratio (υ_c)	0.2
	Ultimate compressive stress (f_c)	27.6 MPa
	Ultimate elastic compressive stress (σ_{0c})	11.04 MPa
	Ultimate tensile stress (f_t)	2.2 MPa
	Strain at the peak compressive stress (ε_{c1})	0.0018
	Ultimate compressive strain (ε_{cu})	0.0034
	Ultimate tensile strain (ε_{tu})	0.002
Reinforcement bar	Mass density (ρ_s)	7800 kg/m^3
	Elastic modulus (E_s)	200 GPa
	Poisson's ratio (υ_s)	0.3
	Yield strength (f_{sy})	400 MPa
	Ultimate strength(f_{su})	500 MPa
	Elastic strain (ε_{sy})	0.002
	Ultimate strain (ε_{su})	0.2

referenced in the literature for earthquake sequences with an interval time.

2. Description of the AP1000 NPP model

2.1. Numerical modeling

The AP1000 is an advanced pressurized water reactor developed by Westinghouse. It is certified by the NRC. The reactor features passive safety systems (PSSR), which operate without the need for external power or operator intervention. Its design allows for safe shutdown without external intervention in case of an emergency. Additionally, its simplified design ensures lower construction and operational costs. The AP1000 NPP comprises essential components such as a steel containment vessel, reinforced concrete containment/shield building, auxiliary building, waste building, and turbine building, as illustrated in Fig. 1. The most critical part of the AP1000 NPP for seismic design is the reinforced concrete shield building (RCSB) since it prevents the leakage of radiation. The AP1000 was chosen for this study due to the abundance of experimental and numerical analyses available in the literature, as well as the accessibility of detailed information through open sources, which facilitated the verification of our numerical work. In this study, we focused on the evaluation of the seismic performances of this structure.

The RCSB is a cylindrical structure. It has a height of 81.54 m, a diameter of 44.2 m, and a wall thickness of 0.914 m. The RCSB has 16 air holes with dimensions of 1.5 m × 2 m in a cylindrical wall with 1.1 m thickness in the upper 9.8 m part of the wall. The basement slab of RCSB has 12 m thickness (). An illustration of AP1000 NPP structures is shown in Fig. 1, and detailed geometries of the RCSB are presented in Table 1. The cylindrical wall is reinforced with a ratio of 0.00306 and a concrete cover of 50 mm (“ACI 349, 2001). It does not include pre- or post-stressed tendons, and the wall details are provided in Fig. 2(a). The concrete utilized in the RCSB has a compressive strength of 27.6 MPa, a tensile strength of 2.2 MPa, and an elastic modulus of 26.3 GPa. The reinforcement bars within the RCSB have a tensile strength of 400 MPa and an elastic modulus of 200 GPa. Detailed material properties are provided in Table 2 (). It should be noted that the primary piping in the vessel was not considered in the numerical model to simplify the calculation.

In finite element analysis (FEA), generally, three typical modeling schemes are conducted. One of them is lumped mass modeling, typically used to obtain global acceleration and displacement responses along the height of structures. The second method involves using solid elements, where each material, such as concrete and steel, can be modeled as

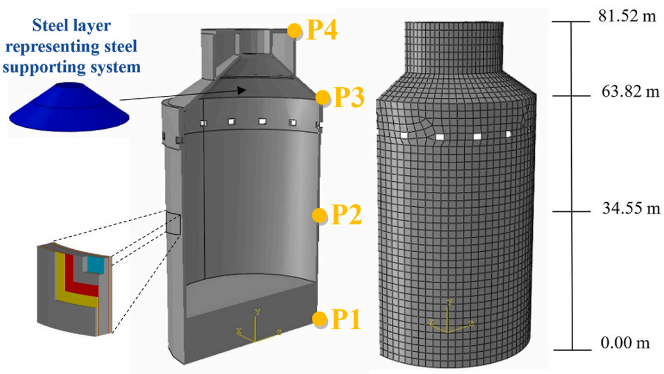

Fig. 3. Numerical model of AP1000 containment building.

separate elements. This type of modeling is essential when the thickness of the material and the interaction between different materials are critical. Another method of simulation is to use layered shell elements. This uses shell elements to represent thin-walled structures that can define embedded rebar and concrete as part of the shell. Layered shell elements are beneficial when simulating structures where bending is significant, and the wall thickness is small compared to other dimensions. The lumped mass approach is particularly useful for seismic analysis, where capturing the global response of the structure is more important than the detailed stress or strain distribution. Solid elements can be computationally expensive, especially when a fine mesh structure is required to capture the variations through the thickness of the material accurately. On the other hand, layered shell elements provide a good balance between accuracy and computational efficiency by reducing the problem dimensions while still capturing the essential behavior of the structure. Thus, the layered shell element method was used in this study.

S4R layered shell elements, characterized by four nodes, dealt with both bending and membrane and using reduced integration, were used in the simulation of the RCSB. These elements model the reinforcing bars efficiently, assuming an optimal bond between the rebars and the surrounding concrete. Each layer defines material properties, spacing of the reinforcement bars, and thickness, capturing the interaction between concrete and reinforcement accurately (Fig. 2). This setup simulates stress transfer and cracking behavior effectively, ensuring realistic predictions of the performance of the reinforced concrete under various loading conditions (Bathe, 1996).

Earthquake records are obtained from bedrock outcrops or free field surfaces; thus, soil-structure interaction was not considered in this study, meaning that all the numerical models of this study were fixed at the bottom. Additionally, the fluid-structure interaction was not considered, and the water tank on the top of the shield building was considered empty. In this study, the accelerations and displacements were measured at four different locations, as shown in Fig. 3.

2.2. Constitutive laws of materials and damage state

In order to achieve reliable computational results, the stress-strain curve formulation, known as the constitutive relationship, is crucial for nonlinear analyses in reinforced concrete structures. This section focuses on presenting the constitutive relationships for both concrete and steel materials utilized in this study to determine corresponding material parameters. In this paper, the constitutive relationship proposed by Yip (1998) was adopted to describe concrete compressive behavior. The concrete stress–strain constitutive relationship in compression is shown in Fig. 4(a). The elastic modulus of the concrete (E_c) is defined as $5{,}000\sqrt{f_c}$. The ultimate elastic compressive stress (σ_{0c}) is $0.4\,f_c$. The stress-strain equation can be expressed as follows (Eq. (1)).

$$\sigma_c = \frac{m\ (\varepsilon_c/\varepsilon_{c1})}{m-1+(\varepsilon_c/\varepsilon_{c1})^{mk}}\,f_c \tag{1}$$

where, m is defined as $m = 0.8 + f_c/17$, and ε_{c1} is the strain at peak stress, is given by $\varepsilon_{c1} = f_c/E_c\cdot(m/(m-1))$, The parameter k depends on the strain ratio and is defined as $k = 1.0$, when $\varepsilon_c/\varepsilon_{c1} \le 1$, $k = 0.67 + f_c/67$ when $\varepsilon_c/\varepsilon_{c1} > 1$. The ultimate tensile and compressive strains are 2.0×10^{-3} and 3.4×10^{-3}, respectively, as reported in literature (Stramandinoli and Rovere, 2008).

The concrete tensile behavior (Lo Frano and Forasassi, 2012) can be expressed by Eq. (2):

$$\sigma_t = f_t e^{\alpha\left(\frac{\varepsilon_t}{\varepsilon_{t0}}\right)} \tag{2}$$

where σ_t and ε_t are the concrete tensile stress and strain, respectively; α is the decay parameter. α and ε_{t0} can be calculated by Eq. (3) and Eq. (4), respectively.

$$\alpha = 0.017 + 0.255(n\rho) - 0.106(n\rho)^2 + 0.016(n\rho)^3 \tag{3}$$

$$\varepsilon_{t0} = f_t/E_c \tag{4}$$

where $n = E_s/E_c$, E_s is the steel elastic modulus, and ρ is the reinforcement ratio. The concrete stress–strain constitutive relationship in tension is presented in Fig. 4(b).

The compression damage factor (d_t) and the tension damage factor (d_c) can be determined by Eq. (5) (Lubliner et al., 1989).

$$d_c = 1-\sqrt{\frac{\sigma_c}{E_c\varepsilon_c}},\quad d_t = 1-\sqrt{\frac{\sigma_t}{E_c\varepsilon_t}} \tag{5}$$

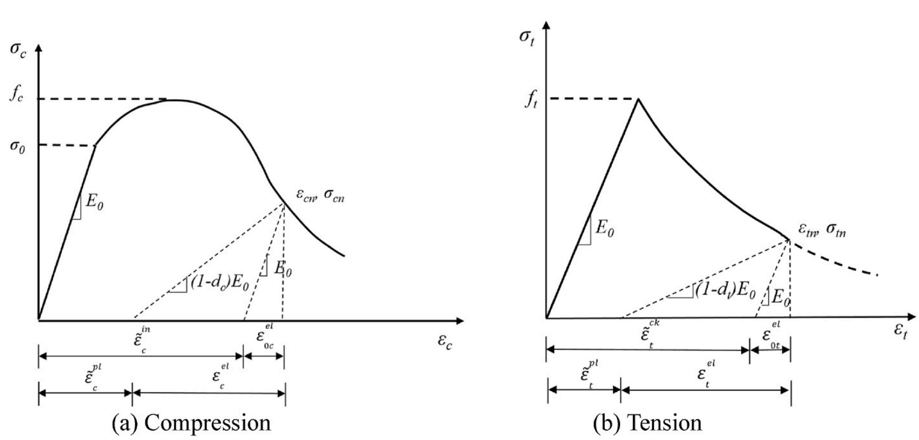

Fig. 4. Stress-strain curve of the concrete damage model.

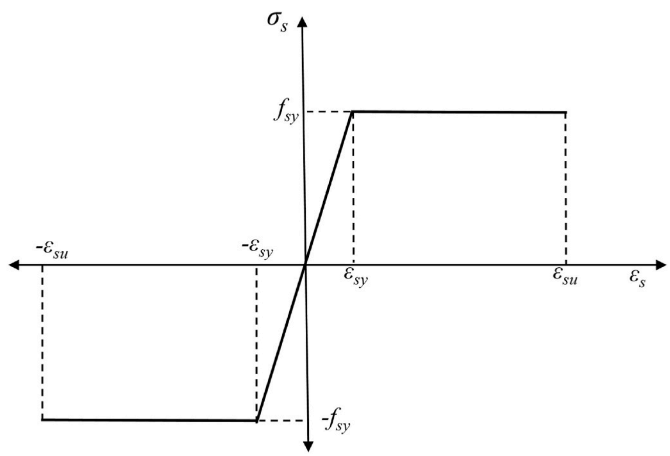

Fig. 5. Stress-strain curve of the bilinear reinforcement model.

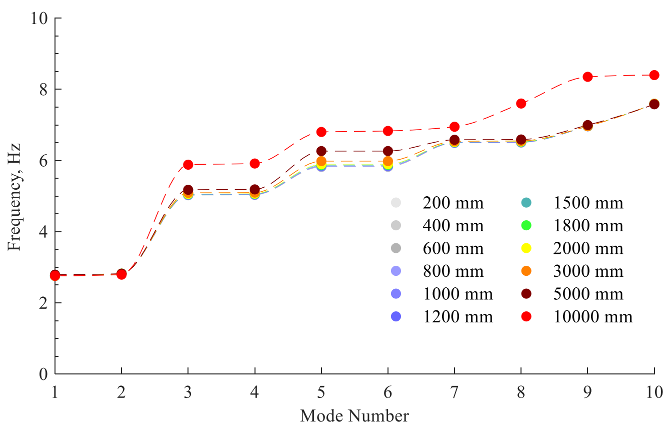

Fig. 6. Convergence of mesh size effects.

The corresponding damage factors are calculated according to the above formulas to obtain the corresponding tension and compression damage factors under different damage states of concrete.

Fig. 5 shows the bilinear model of the reinforcement. The stress–-strain relationship of the reinforcing bar can be expressed by Eq. (6):

$$\sigma_s = \begin{cases} E_s.\varepsilon_s(\varepsilon_s < \varepsilon_{sy}) \\ f_{sy}(\varepsilon_{sy} \le \varepsilon_s \le \varepsilon_{su}) \end{cases} \tag{6}$$

where σ_s and ε_s are the steel stress and strain, respectively.

2.3. Convergence analysis

Before conducting dynamic analysis, a mesh convergence analysis is performed to determine the appropriate mesh element size, as the mesh size influences the accuracy of numerical results. Generally, adopting a smaller mesh size can simulate more accurate results. However, employing minimal element sizes is impractical because it significantly increases computational costs. In this study, mesh sizes of 200, 400, 600, 800, 1000, 1200, 1500, 1800, 2000, 3000, 5000, and 10000 mm were tested, most of which comply with ASCE 4–16 requirements ("ASCE/SEI 4, 2017).

For the convergence analysis, the results of the modal analysis of the RCSB structure with varying mesh sizes are presented in Fig. 6. The discrepancies in the modal analysis results between the 200 mm and 2000 mm mesh sizes were only about 1%. Meanwhile, mesh sizes of 5000 mm and 10000 mm exhibited errors of more than 7% and 20%, respectively, compared to the smaller mesh sizes. Based on the convergence analysis results, a mesh size of 1800 mm was selected. Additionally, mesh sizes of 800 mm and 1800 mm were evaluated using dynamic analysis. The acceleration and displacement response errors were lower than 4% and 3%, respectively.

2.4. Modal analysis

Mode shapes and frequencies are crucial in structural analysis for understanding how structures behave under dynamic loads. Natural frequencies indicate the specific frequencies at which a structure tends to vibrate. Determining the natural frequencies helps to avoid resonance that can cause significant damage. Mode shapes show how a structure deforms or moves during vibration, revealing movement patterns under dynamic loads. Effective mass and rotational effective mass are also essential. Effective mass represents the portion of the total mass involved in a specific vibration mode, while rotational effective mass considers how mass distribution influences rotational movements. These concepts help identify critical modes affecting the structure's response to dynamic loads.

To determine the effective mass of modes, the guidance provided by Chopra (1995) was adopted to ensure precise simulations and efficient damping system design under dynamic forces. The first and second modes exhibit significant effective mass and rotational effective mass ratios at a frequency of 2.76 Hz. In the modal analysis of the structure, it was observed that certain modes exhibited negligible participation factors, indicating primarily local responses, largely due to the shape of the structure. To ensure that the cumulative effective mass of the structure reached at least 75%, 22 modes were included in the analysis. Mode shapes with more than 15% effective mass ratios are illustrated in Fig. 7, highlighting the most critical modes for the structure's dynamic

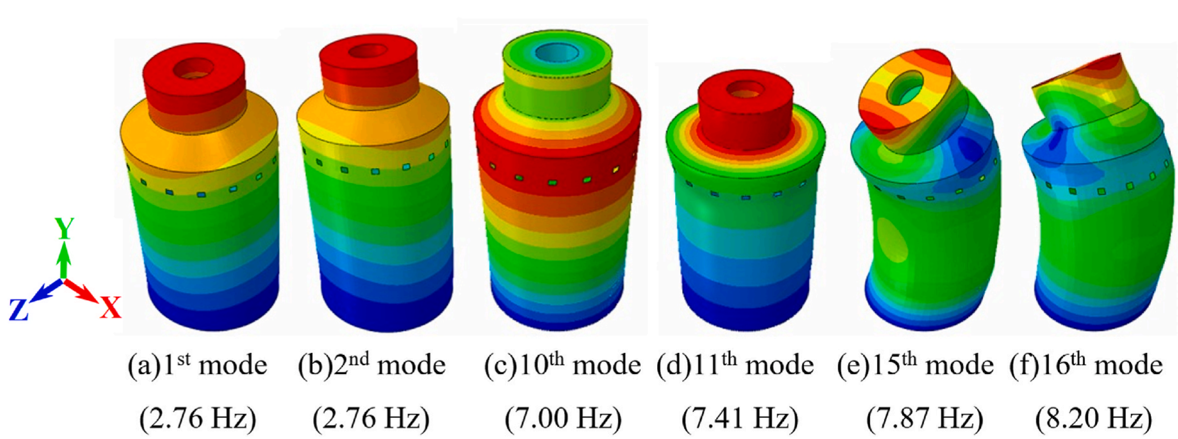

Fig. 7. Mode shapes of the structure.

behavior.

2.5. Equation of motion of system and damping ratio

Equation of motion of the structure system subjected to an earthquake force is essential in numerical modeling for predicting the structural dynamic behavior, typically expressed by Eq. (7).

$$\mathbf{M}\{\ddot{u}\} + \mathbf{C}\{\dot{\mathbf{u}}\} + \mathbf{K}\{u\} = \mathbf{M}\ddot{u}_g(t) \tag{7}$$

where **M** is the mass matrix, **C** is the damping matrix, **K** is the stiffness matrix; u, $\dot{\mathbf{u}}$, $\ddot{u}$ are the displacement, velocity and acceleration vectors respectively; and $\ddot{u}_g$ (t) is the ground motion acceleration. For modeling damping, the Rayleigh damping ratio is commonly used. This method assumes the damping matrix C is a combination of the mass and stiffness matrices, calculated by Eq. (8).

$$\mathbf{C} = \alpha\mathbf{M} + \beta\mathbf{K} \tag{8}$$

where α and β are the Rayleigh damping coefficients, which link damping to the system's mass and stiffness properties, simplifying the integration of damping effects in numerical simulations. The coefficients α and β are determined based on the desired damping ratios at specific frequencies. Typically, the values of α and β are calculated using the following equations:

$$\alpha = \frac{2\zeta\omega_1\omega_2}{\omega_{1+}\omega_2} \tag{9}$$

$$\beta = \frac{2\zeta}{\omega_{1+}\omega_2} \tag{10}$$

where ζ represents the damping ratio, while ω_1 and ω_2 are the circular frequencies of the first and second modes of the AP1000 RCSB structure, respectively.

In this study, the damping ratio was selected as 5%. As described in the Regulatory Guide (RG) 1.61 ("RG 1, 2007) and ASCE 43-05 ("ASCE/SEI 43, 2005), the estimated damping ratio depends on the demand-to-capacity ratio (D_e/C). Since the study aimed to evaluate various seismic conditions, including Operating Basis Earthquake (OBE), Safe Shutdown Earthquake (SSE), and Safe Shutdown Margin Earthquake (SME), a 5% damping ratio was chosen for reinforced concrete materials. This selection was made to enable the comparison of results under different seismic conditions.

In the dynamic analysis, gravity was defined in the first step. In the second step, combined earthquakes were applied using multiple interval baseline corrections. Initially, the model was subjected to artificial earthquakes (AEs), which were matched to the RG 1.60 design spectrum. Next, a series of sequential ground excitations during the 2023 Türkiye earthquake were applied. The results of each combined earthquake analysis were compared to those obtained from the AEs and were also assessed against safety parameters. Additionally, these results of the combined earthquake analysis were compared with the results obtained immediately after the Pazarcık earthquake phase within the same analysis. In case differences were observed, the Elbistan and Yayladağı earthquakes were applied separately to the model. This approach enabled a comparison to determine the specific impact of each aftershock in the sequence.

2.6. Earthquake input

The AEs were applied to the base of the numerical structure in three orthogonal directions (two horizontal and one vertical) in accordance with ASCE 4–16 ("ASCE/SEI 4, 2017), with peak PGA ratios of 1:1:0.67 for horizontal and vertical components, respectively. Similarly, real-time earthquake records were applied in the same three orthogonal directions using their recorded accelerograms.

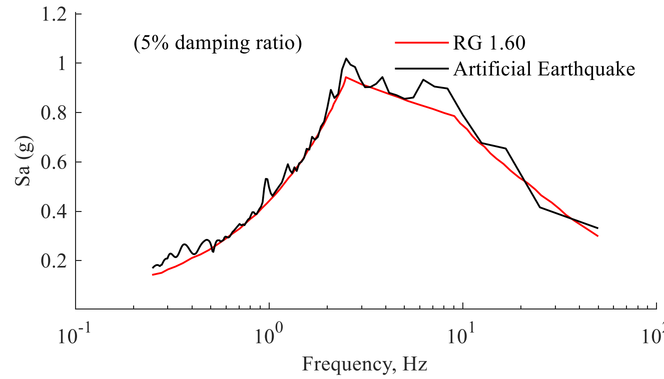

Fig. 8. The response spectrum of artificial wave (PGA 0.30g).

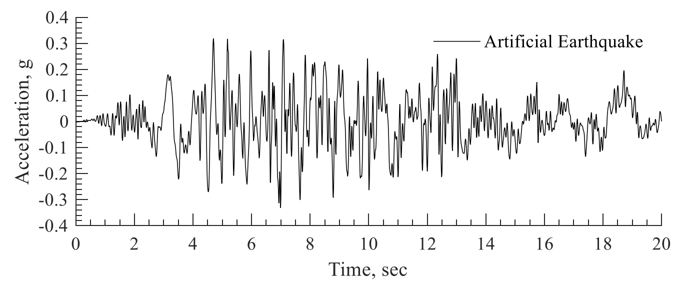

Fig. 9. Artificial RG 1.60 acceleration.

2.6.1. Design base earthquakes

The seismic design of NPPs is based on the likelihood of certain events occurring over specific timeframes. The SSE level, expected once every 10,000 years, serves as a design criterion mandating that critical structures, systems, and components (SSCs) maintain functionality during and after such an event to ensure plant safety under extreme conditions. The OBE level, occurring once every 100 years, ensures the plant can withstand moderate seismic events without compromising safety, with ground motion values set at one-half or one-third of the SSE (Kennedy, 1985). Kennedy et al. ("ASCE/SEI 43, 2005) used the term "seismic margin earthquake" to describe an earthquake with ground motions larger than the SSE and recommended using a margin factor 1.67 times the SSE. SME, with a probability of once in 100,000 years, provides an extra safety margin for extremely rare and intense events.

In seismic evaluations, the SSE sets the upper boundary for seismic design, maintaining the functionality of critical SSCs during and after the event. However, the SMA employs the Review Level Earthquake (RLE) as its seismic benchmark, which is required to surpass the SSE. According to the EPRI NP-6041 report (Methodologies for Seismic Safety Evaluation, 2020), the SME is considered equivalent to the RLE, as defined by NUREG-1407 (Newmark and Hall, 1991).

Ground motion response spectra, such as those from RG 1.60 ("RG 1, 2014), incorporate probabilistic seismic hazard assessments, providing realistic input for design. Synthetic earthquakes generated to match these spectra offer deterministic inputs for time history analysis, ensuring consistency with design criteria. According to several researchers and regulations, sites are categorized based on PGA into three groups: PGA $\leq$0.30g, 0.30g $<$ PGA $\leq$0.50g, and PGA $>$0.50g, with reference levels at 0.30g, 0.50g, and greater than 0.50g, respectively (Seismic Hazard Evaluations for, 2021), ("ASCE/SEI 4, 2017), ("ASCE/SEI 43, 2005), (Kennedy, 1985). For analysis purposes, artificial earthquakes based on RG 1.60 can be used with 0.30g of PGA corresponding to the SSE level. As described above, for OBE and SME, the PGA can be selected with one-half or one-third and more than 1.67 times the PGA of SSE, respectively (Kennedy, 1985). Using RG 1.60 (Fig. 8), an artificial earthquake was obtained using the SeismoArtif software,

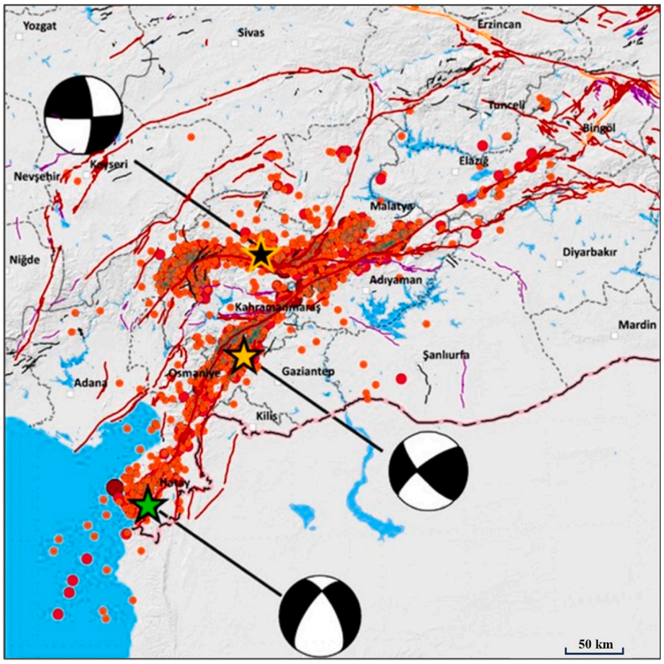

Fig. 10. Pazarcık, Elbistan, and Yayladağı earthquakes and aftershock activity (Zengin and Aydin, 2023).

which generates artificial earthquake records (Fig. 9) matching the design spectrum. This approach ensures that the generated ground motions are consistent with the specified design criteria, providing a robust basis for seismic analysis and design. In this study, the artificial earthquake was utilized to represent the OBE, SSE, and SME with ground motion values of 0.15g, 0.30g, and 0.50g, respectively, with a peak PGA ratio of 1:1:0.67 for the horizontal and vertical directions. These were labelled as AE 0.15, AE 0.30, and AE 0.50.

2.6.2. Real-time earthquakes

On February 6, 2023, two major earthquakes struck south-central Türkiye near the Türkiye-Syria border. At first, the Pazarcık earthquake occurred at 4:18 a.m. with a magnitude of M_w 7.7. About 9 h later, the Elbistan earthquake struck to the north with a magnitude of M_w 7.6. Two weeks later, Hatay, already affected by the initial quakes, experienced another earthquake (Yayladağı) with a magnitude of M_w 6.4, as illustrated in Fig. 10. These seismic events occurred near the Maraş seismic gap and along the East Anatolian fault, an active strike-slip fault formed by the collision between the Anatolian and Arabian plates (Jiang et al., 2023).

To investigate the dynamic response of RCSB under three consecutive earthquakes, 12 ground motion records were selected in different stations, as shown in Fig. 11. It should be noted that the stations with the highest PGAs for three single earthquakes were chosen. Additionally, the stations were selected based on their proximity to water sources rather than solely on areas where PGAs were relatively high. Most of those selected stations are near the Mediterranean Sea, while some stations are near streams or ponds. These accelerograms were then used in numerical simulations. General information about the selected earthquake recording stations is provided in Table 3, while Table 4 illustrates the PGA of these earthquakes. In this study, the notations of the stations were used as their original name assigned by the Turkish Accelerometric Database and Analysis System (TADAS). In the station name, the first two digits represent the code of the city as 01 Adana, 27 Gaziantep, 31 Hatay, 33 Mersin, 46 Kahramanmaraş. The subsequent two digits are assigned to specific stations within these cities.

Combined earthquake excitations are indicated by codes such as 'C0119', 'C3125', or 'C4612'. In these codes, the letter 'C' signifies 'combined', followed by digits that represent the specific station records utilized in the analyses. Additionally, in combined earthquake excitation analysis, the immediate propagation of dynamic stress changes is followed by stress redistribution. This process necessitates an interval—typically ranging from 10 to 100 s—between the main shock and subsequent shocks. This interval is determined based on the specific objectives and the time duration of the earthquake being analyzed.

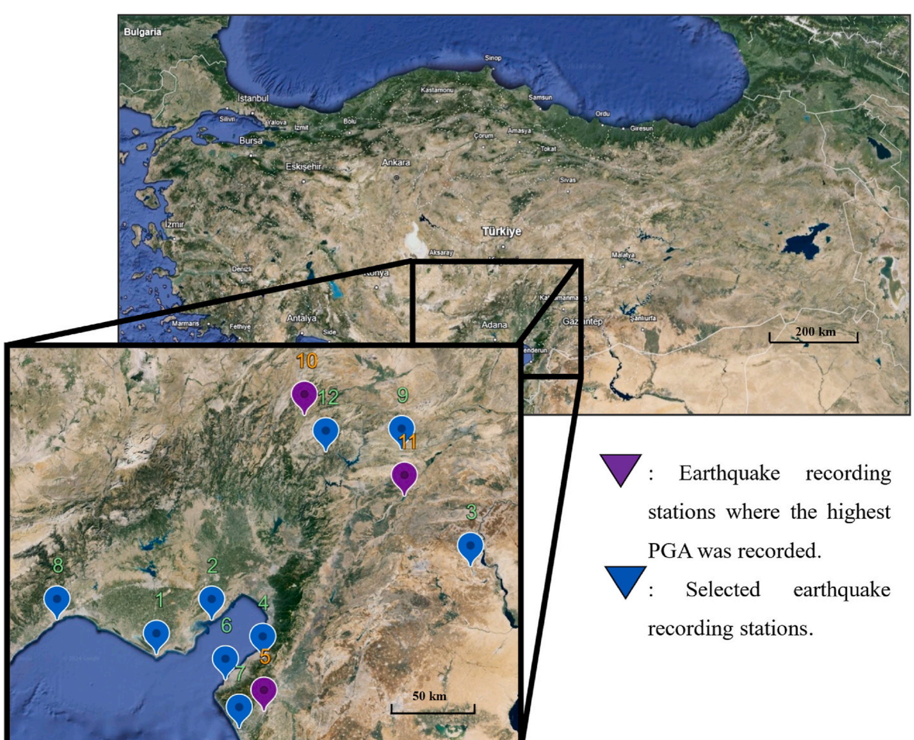

Fig. 11. Selected earthquake recording stations.

Table 3
General information of selected earthquake recording stations.

No	Code	Longitude	Latitude	Province	District	V_{s30} (m/s)
1	0119	35.39	36.57	Adana	Karataş	280
2	0120	35.79	36.77	Adana	Yumurtalık	541
3	2704	37.8	37.01	Gaziantep	Nizip	731
4	3115	36.16	36.55	Hatay	Belen	721
5	3125	36.13	36.24	Hatay	Antakya	246
6	3135	35.88	36.41	Hatay	Arsuz	424
7	3140	35.95	36.08	Hatay	Samandağ	439
8	3301	34.6	36.78	Mersin	Yenişehir	460
9	4611	37.28	37.75	Kahramanmaraş	Çağlayancerit	448
10	4612	36.48	38.02	Kahramanmaraş	Göksun	210
11	4614	37.3	37.49	Kahramanmaraş	Pazarcık	486
12	4624	36.92	37.54	Kahramanmaraş	Onikişubat	367

Table 4
Recorded peak ground accelerations and epicenters of three earthquakes.

No	Code	Pazarcık				Elbistan				Yayladağı			
		PGA NS	PGA EW	PGA UD	R_{epi} (km)	PGA NS	PGA EW	PGA UD	R_{epi} (km)	PGA NS	PGA EW	PGA UD	R_{epi} (km)
1	0119	0.04	0.05	0.03	167	0.01	0.01	0.01	235				
2	0120	0.11	0.12	0.11	125	0.02	0.03	0.02	195	0.03	0.02	0.01	84
3	2704	0.1	0.16	0.07	74	0.04	0.06	0.02	130	0.01	0.02	0.01	192
4	3115	0.29	0.25	0.22	113	0.03	0.03	0.02	196	0.11	0.12	0.07	58
5	3125	**0.84**	**1.14**	**1.17**	142	0.03	0.02	0.02	228	**0.79**	**0.78**	**0.47**	**25**
6	3135	**0.76**	**1.4**	**0.6**	142	0.02	0.02	0.01	222	0.36	0.35	0.21	43
7	3140	0.2	0.22	0.18	165	0.03	0.03	0.02	251	0.18	0.17	0.15	8
8	3301	0.03	0.05	0.02	224	0.02	0.02	0.01	274				
9	4611	0.36	0.33	0.18	55	0.2	0.14	0.07	38				
10	4612	0.14	0.12	0.06	95	**0.65**	**0.53**	**0.5**	67	0.01	0.01	0	225
11	4614	**2.21**	**2.22**	**1.99**	31	0.16	0.21	0.09	67	0.01	0.01	0	197
12	4624	0.36	0.32	0.16	30	0.07	0.08	0.04	68	0.02	0.02	0.01	185

■: < 0.1g, ■ : 0.1g-0.15g, ■: 0.15g-0.3g ■:0.3g-0.5g ■: > 0.5g

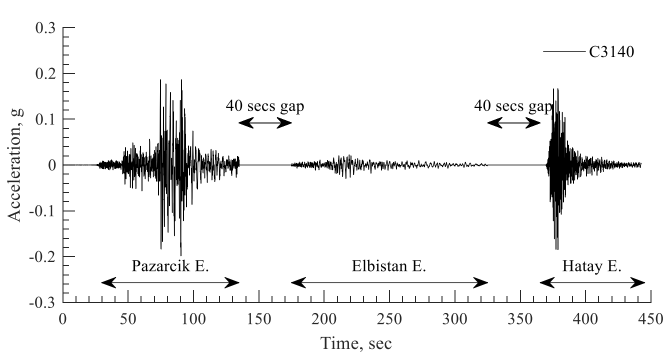

Fig. 12. Earthquake input of C3140 in the X direction.

During this interval, the structure is assumed to remain static and stationary before the onset of the aftershock. In this study, to ensure computational efficiency and analytical accuracy, a 40-s interval was introduced between the main shock and subsequent shocks, as illustrated in Fig. 12.

2.7. Safety parameters and limit states

According to ASCE 43-05 ("ASCE/SEI 43, 2005), various limit states

Table 5
Structural deformation limit for limit state ("ASCE/SEI 43, 2005).

Limit State (LS)	Structural Deformation Limit	
A	Large permanent distortion, short of collapse *Significant damage*	SME
B	Moderate permanent distortion *Generally repairable damage*	SSE
C	Limited permanent distortion *Minimal damage*	OBE
D	Essentially elastic behavior *No damage*	

(LSs) and their corresponding deformation criteria are outlined in Table 5. As described by Murphy et al. (Murphy and Tegeler, 2007), the Design Safe Earthquake (DSE), OBE, SSE, and SME can be employed as LSs for NPP designs (Li and Zhang, 2013). For some NPP models, the OBE is considered to induce only limited permanent distortion. In contrast, the SSE is associated with moderate permanent distortion. Additionally, in a few NPP models, the SME level is deemed to be capable of causing devastating impacts. For this reason, SME, SSE, and OBE were adopted as the limits for A, B, and C, respectively, in this study.

After conducting the analysis of the model under AEs, the obtained damage indexes are presented in Table 6. Maximum tension and

Table 6
Damage index.

Damage Factor	Damage index			
	Elastic 0	Light Damage (0, AE 0.30]	Controlled Damage (AE 0.30, AE 0.50)	Severe Damage ≥ AE 0.50
d_t	0	(0, 0.70]	(0.70, 0.884)	≥0.884
d_c	0	(0, 0.001]	(0.01, 0.1)	≥0.552

Table 7
Allowable drift and nonlinear hinge rotation limits as a Function of limit state and structural systems ("ASCE/SEI 43, 2005).

Limit State	Allowable Drift Limit, γ_a			
	LS-A	LS-B	LS-C	LS-D
Reinforced concrete shear wall, in plane: Bending controlled walls,	0.008	0.006	0.004	0.004
	Allowable Nonlinear Hinge Rotation, θ_A			
Limit State	LS-A	LS-B	LS-C	LS-D
Slab/wall moment frame: Roof slabs, floor slabs, beams, and walls of reinforced concrete	0.0075	0.006	0.005	–

compression damage factors (d_t and d_c, respectively) from the AE analyses were used to define LSs of damage factors under seismic loading. Furthermore, the results of AEs were also used as LSs for evaluating the peak floor accelerations (PFA), maximum relative displacements (MRD), and damage dissipated energy outcomes from cases involving actual combined earthquakes.

As described in ASCE 43-05 ("ASCE/SEI 43, 2005), the linear analyses utilize strength acceptance criteria, while the nonlinear analyses are expected to meet deformation acceptance criteria. For deformation acceptance, allowable drift limit and allowable nonlinear hinge rotation limit criteria (in Table 7) were used to evaluate the results. The structure does not have stories with relatively higher masses, unlike frame structures that can exhibit opposite mode shape components in the mode shape factors, causing reverse movement in the mode shapes. Therefore, the allowable drift ratio was used to compare the MRD of each floor from the ground floor. Hinge rotation refers to the angular displacement that occurs at a hinge point within a structure, allowing it to rotate. In finite element modeling (FEM), hinge rotation refers to the rotational displacement at a node, allowing for an angular movement similar to the hinge point within the structures.

Additionally, in this study, two strain-associated LSs were proposed to assess the structural integrity of reinforced concrete components under seismic loads. The maximum principal strain limit is related to the onset of concrete cracking, identified by the first principal strain (typically tensile) reaching 0.001. This LS, which accounts for the strain-softening behavior of concrete under tension, is endorsed by notable researchers such as Moon et al. (2012), This approach is also recommended by the FEA software ABAQUS ("ABAQUS/CAE User). Reaching that allowable limit indicates cracking occurs through the thickness of the containment structure.

The minimum principal strain limit relates to concrete crushing, defined by the third principal strain (usually compressive) reaching 0.003. This value is significant for concrete layers under plane stress conditions within the containment wall, where the ultimate compressive strain under biaxial loading slightly differs from that under uniaxial compression. Comparable values of 0.003 and 0.0035 are also suggested in authoritative sources, including textbooks and international codes (Lin and Li, 2017; "CEB-FIP Model Code, 2010, 2010; Wight and MacGregor, 2011).

Table 8
Overview of the experimental model and the prototype.

Parameter	Prototype	Model
Height	71.10 m	1.78 m
Diameter	44.20 m	1.10 m
Thickness	0.92 m	0.01 (not to scale) m
Material	Steel	Plexiglass

3. Verification of numerical model

An experiment implemented by Zhao et al. (2023) was used to verify the numerical modelling in this study. They conducted an experimental shaking table test on a 1:40 scale model of the AP1000 NPP containment building using the Buckingham-π theorem together with the shaking table test design method proposed by Zhang et al. (Zhang, 1997). The geometrical parameters of the 1:40 scale model and a prototype of the full-scale model are given in Table 8. In the experimental test, to meet the frequency similarity ratio, a steel plate with additional mass blocks (1524 kg in total) was placed at the base of the structure, and counterweights of 75 kg, 150 kg, and 115 kg were distributed over three floors of the superstructure, as shown in Fig. 13. These additional weights were also considered in the numerical analysis. The steel bars, which represent a non-isolated system, have dimensions of 100 and 150 mm and a total height of 342 mm. The concrete foundation has a thickness of 100 mm and a diameter of 600 mm.

In the experiment, the material properties and details of the parts were assigned, as shown in Fig. 13. Plexiglass was used to represent the wall of the containment according to the scaling factor. Concrete was used for the foundation of the structure, while additional weights, the base plate, and steel bars for non-isolated systems were defined as steel components. The research paper did not specify the material properties of the steel, concrete, and plexiglass. Therefore, typical and widely accepted properties for steel, concrete, and plexiglass from the literature were adopted. Table 9 presents these material properties.

The steel plate and the plexiglass wall of the containment were divided into S4R shell element meshes with a 30 mm mesh size, while C3D8R solid elements with the same mesh size were used for the other components. For shell plate and containment, node-to-node connections were defined by merging them into a single part; for other separated parts, surface-to-surface tie connections were used. In the experimental test, an artificial earthquake based on RG 1.60 ("RG 1, 2014) was used, obtained by applying a scaling factor to the PGA at the SSE level, with a PGA ratio in the horizontal and vertical directions of 1:1:0.67. In the numerical simulation, a similar artificial earthquake profile, as detailed in Section 2.6.1, was used with the same PGA described in the experimental setup.

The results of the frequency analysis are given in Table 10. The first three modes tended to be in three different directions, X, Z, and Y, respectively, as shown in Fig. 14. It can be found that the numerical results are comparable to that of the experiment, in which the differences were approximately 0.36% in both horizontal and vertical directions.

The peak acceleration magnification factor (PAMF) can reflect the magnification of the acceleration response of the structural system in relation to the intensity of the input motion. The numerical study yielded results comparable to those of the experimental test, as shown in Table 11. The largest difference between the numerical and experimental results was found in the bottom steel plate of the structure, with an error of 10.4%. For other levels, the differences were less than 6%. Consequently, the numerical model can represent the experimental model as a behavior of acceleration response under the 1.60 RG artificial earthquake.

In the experiment, researchers used plexiglass. For this study involving full-scale models with reinforced concrete materials, it is crucial to verify the concrete material model, which was not utilized in

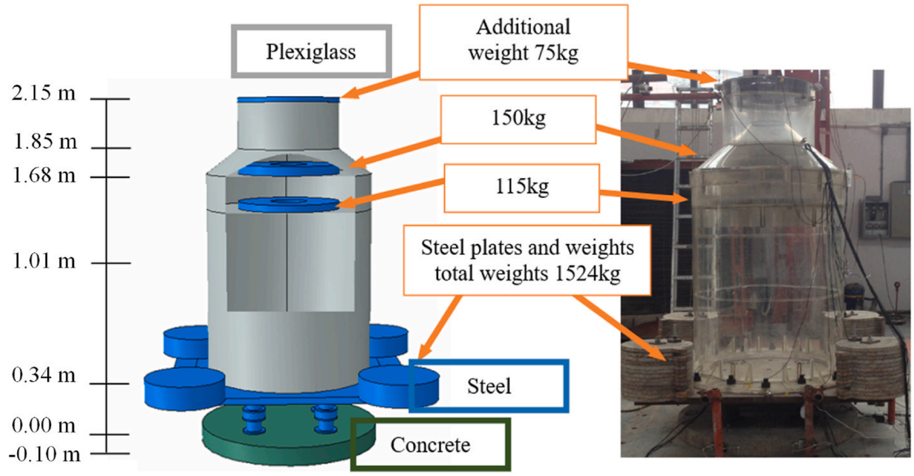

Fig. 13. 1:40 scaled models of AP1000 for experimental and numerical studies.

Table 9
Material properties of the structure.

Material	Elastic modulus	Poisson ratio	Density
Plexiglass	2.6 GPa	0.35	1.17 kg/cm^3
Steel	200 GPa	0.3	7.75 kg/cm^3
Concrete	30 GPa	0.2	2.4 kg/cm^3

Table 10
Natural frequencies of numerical model.

Direction	Natural Frequency, Hz		
	Experimental	ABAQUS	Error %
X (horizontal)	11.25	11.29	0.36
Z (horizontal)	11.25	11.29	0.36
Y (vertical)	19.45	19.52	0.36

the experimental research. Lin et al. (Lin and Li, 2017) conducted a numerical study on a reinforced concrete containment shield building subjected to strong earthquakes and subsequent tsunami effects. In their study, one of the cases of the shield building neglecting tsunami effects (depicted in Fig. 16) was used to verify the constitutive relationship, mesh generation, and solving method. Detailed information on the model's geometry and materials can be referred in Lin et al. (Lin and Li, 2017). The Whittier Narrow-01 earthquake recorded at the Vasquez Rocks Park station was used as the input load, as shown in Fig. 15, with a PGA ratio in the horizontal and vertical directions of 1:1:0.67. To obtain similar results for the first principal strains, a PGA level of 1.1g was scaled and analyzed, consistent with the literature (Lin and Li, 2017). Additionally, another PGA level of 1g was utilized to determine the MRD.

The first principal strain obtained in this study was 0.00106 at the bottom of the structure, indicating a 0.9% deviation compared to the literature (Lin and Li, 2017), as depicted in Fig. 16. Similarly, the errors in MRD at different heights were all smaller than 10%, as illustrated in Table 12. These validation results emphasized that the numerical model used in this study is capable of producing reliable results for future analyses.

4. Results and discussion

This section presents the results and discussion of the numerical analysis of the structural dynamic responses, plastic damage characteristics, strain states, damage dissipated energy, and mainshock-aftershock effects on RCSB subjected to three significant earthquakes in Türkiye. The performance of the RCSB structure was evaluated by focusing on the twelve used earthquake records, which were presented in Section 2.6.2. The results were compared against the allowable limit criteria described in Section 2.7 to ensure safety and compliance. Additionally, the RCSB numerical model was subjected to three artificial earthquakes, as described in Section 2.6.1, to ensure the numerical

Table 11
PAMFs for experimental test and numerical analysis under 1.60 RG acceleration.

Distance (m)	Numerical	Experimental	Error %
0.00	1.00	1.00	–
0.34	1.24	1.37	**10.4**
1.01	2.00	1.88	**6.0**
1.68	3.42	3.27	**4.5**
2.15	4.74	4.89	**3.0**

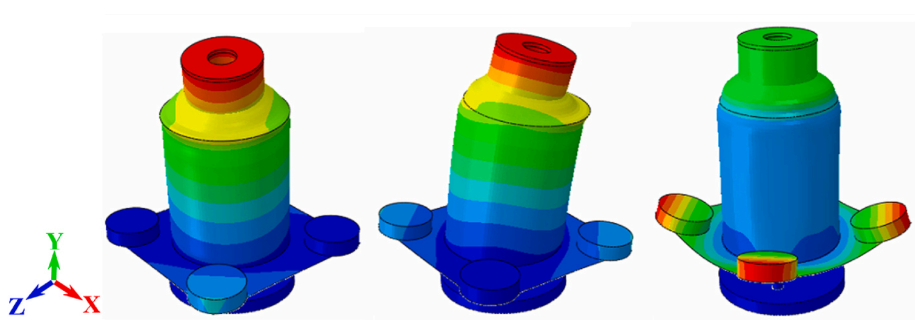

Fig. 14. The first three mode shapes of numerical analysis.

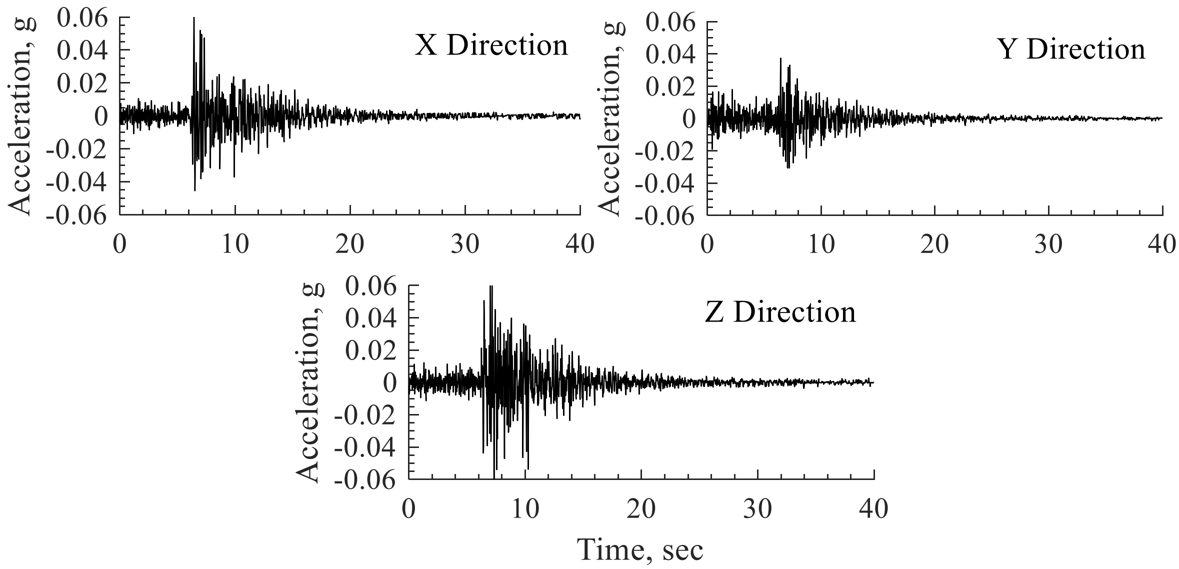

Fig. 15. The Whittier Narrow-01 earthquake wave, recorded in the Vasquez Rocks Park station.

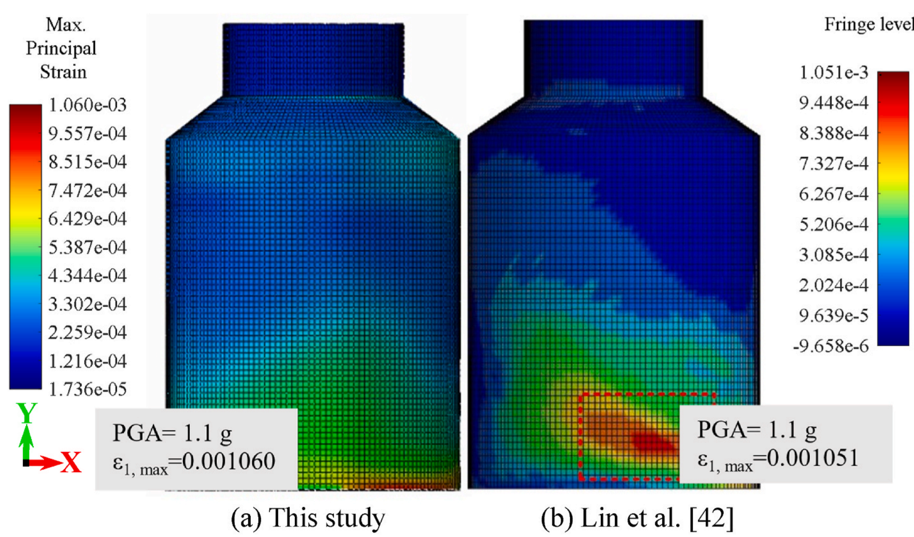

Fig. 16. First principal strains comparison.

Table 12
Comparison of MRDs of containment building.

Height (m)	MRD in X-direction, mm		
	This study	Lin et al. (Lin and Li, 2017)	Error %
0	0.00	0.00	-
10	6.00	6.22	**3.53**
20	10.60	9.92	**6.81**
30	14.43	13.13	**9.93**
40	20.40	18.63	**9.55**
52.6	28.24	27.33	**3.32**
69.6	34.29	35.50	**3.40**

results are reliable. This comparative analysis was essential for assessing the seismic vulnerability of various locations in Türkiye, particularly those near water sources.

4.1. Structural dynamic responses

4.1.1. Acceleration responses

Since NPP facilities contain potentially hazardous materials, such as radioactive substances, seismic safety must be ensured during seismic events. These facilities are generally divided into two categories: acceleration-sensitive and deformation-sensitive ones. This section presents PFAs at various heights within the RCSB, as shown in Fig. 3. Analyzing different floor PFAs under various earthquake excitations revealed significant variability in their responses. Fig. 17 illustrates the maximum acceleration in horizontal and vertical directions across different heights for different cases.

It was observed that high accelerations were obtained in the case of C4614, with values of around 3.9g, 5.24g, and 3.83g in the X, Y, and Z directions, respectively, at the top of the building. These values are significantly higher than the SME level, which corresponds to AE 0.50 values. For cases with PGA higher than AE 0.50, specifically C4612, C3125, C3135, and C4614, higher PFAs were observed, except for C4612. In the case of C4612, in the X direction, the PFA increased from 0.65g to 1.25g on the top floor, compared to an increment from 0.5g to

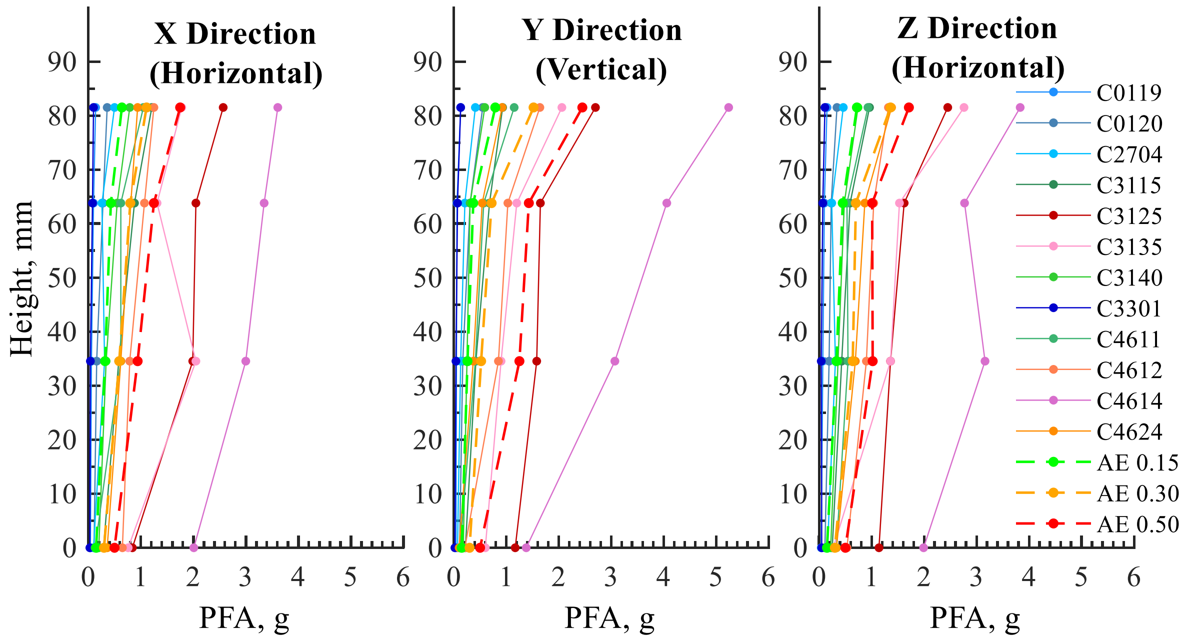

Fig. 17. Peak floor accelerations.

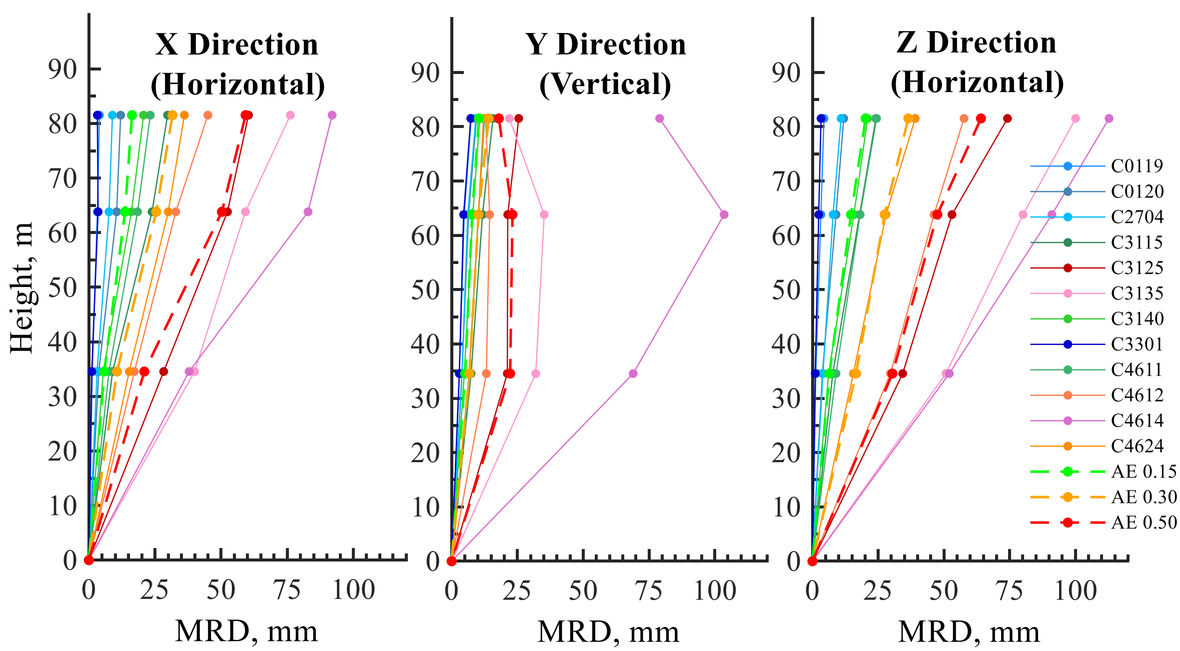

Fig. 18. Maximum relative displacements.

1.75g in the case of AE 0.50. However, even though PFAs were larger in these cases, their PAMFs, i.e., the ratio of PFA to PGA, were lower than the PAMFs of AE 0.50.

For the OBE level, the PFAs at the top point due to AE 0.15 were monitored with 0.64g, 0.79g, and 0.72g in the X, Y, and Z directions, respectively. Meanwhile, the top point accelerations in the X, Y, and Z directions were found to be 0.50g, 0.40g, and 0.46g in these cases of C0119, C3301, C0120, and C2704, respectively, highlighting smaller values compared to those of AE 0.15. Notably, the PAMFs were higher in C0119, C3301, C0120, and C2704, especially in the vertical direction, probably due to the absence of visible plastic deformations.

In other cases, such as C3115, C4611, C4612, and C4624, it was revealed that floor accelerations were comparable with those due to AE 0.30 (i.e., matching SSE level), which recorded peak accelerations of 1.11g, 1.52g, and 1.36g in the X, Y, and Z directions, respectively. Moreover, the PAMFs were observed to be lower compared to the results of AE 0.30.

4.1.2. Displacement responses

Fig. 18 shows the MRDs in the directions X, Y, and Z across different stations. Relative displacement is defined as the movement of each floor compared to the ground floor. The highest displacements were observed at C4614 with 101.0 mm, 118.0 mm, and 112.8 mm in the X, Y, and Z directions, respectively. Significant displacements were also recorded in the cases of C3135 and C3125, exceeding the SME level results. Stations C3140 and C4611 showed acceptable MRDs compared to SSE levels.

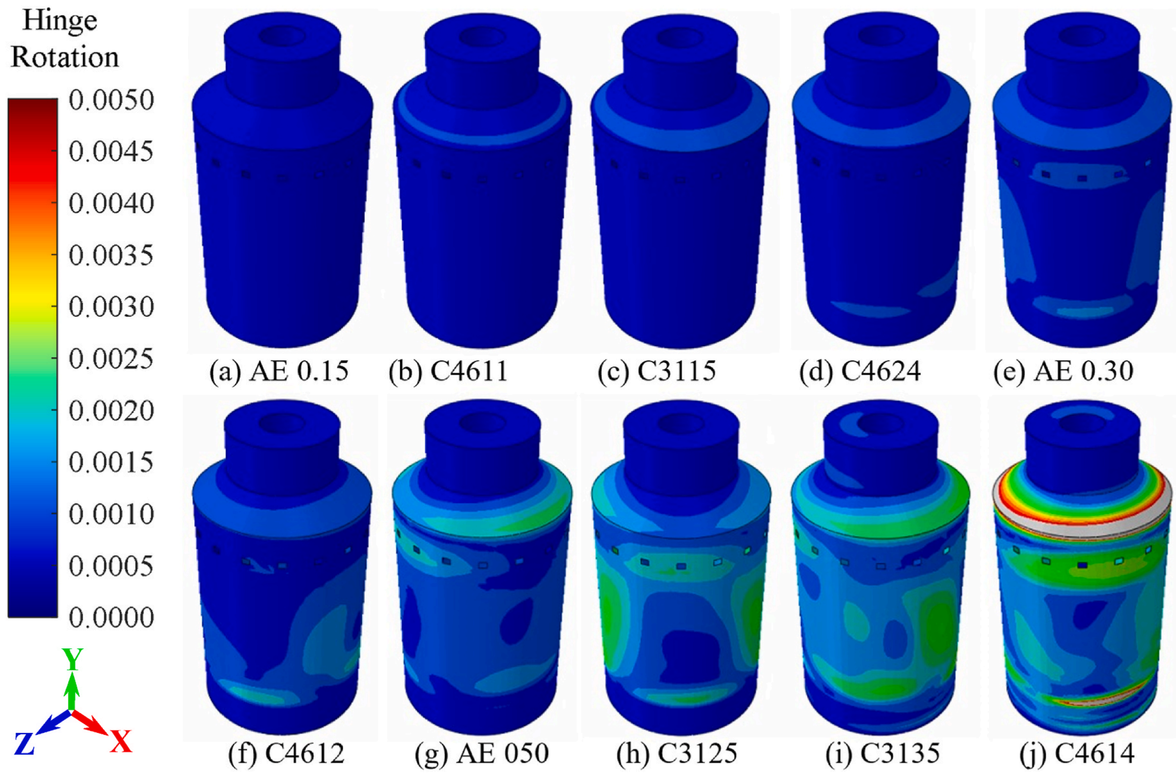

Fig. 19. Nonlinear hinge rotations.

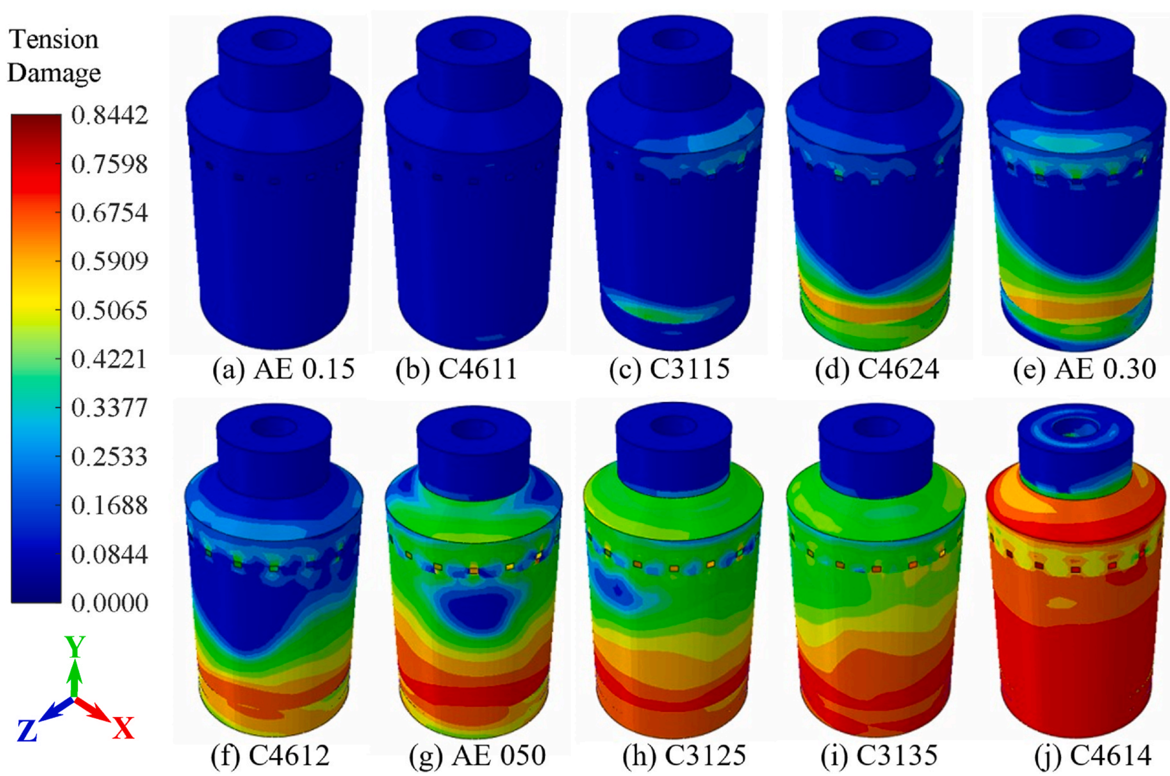

Fig. 20. Tension damage contours.

Combined earthquakes such as C3301, C0119, C0120, and C2704 exhibited relatively lower displacements in all directions compared to the AE 0.15 level, which showed peak MRDs of 19.8 mm horizontally and 10.6 mm vertically. For cases C3125, C3135, and C4614, when MRDs in the vertical direction were analyzed, the highest MRD values were observed at the P3 point, located at a height of 63.82 m. At the top of the RCSB, represented by the P4 point, the MRDs were lower than those at P3. Upon examining Figs. 19–21, this phenomenon was

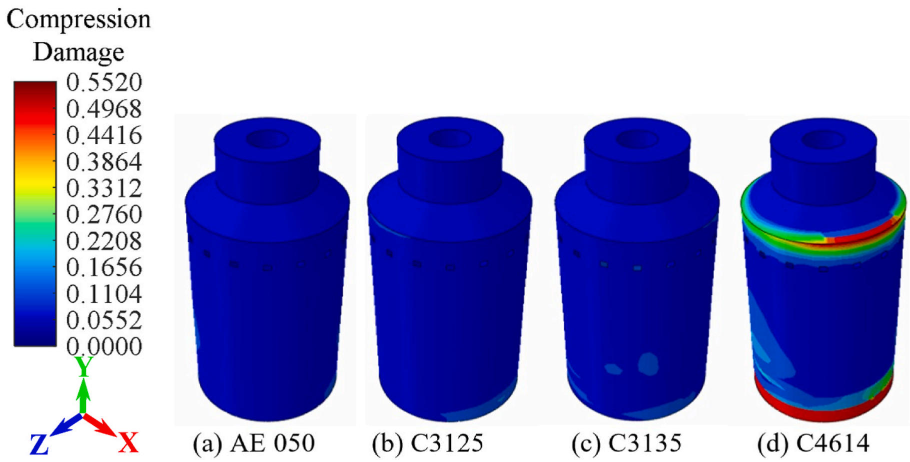

Fig. 21. Compression damage contours.

Table 13
Damage parameters.

Case	Damage			
	d_t	Damage index	d_c	Damage index
C3301	0	*No damage*	0	*No damage*
C0119	0	*No damage*	0	*No damage*
C0120	0	*No damage*	0	*No damage*
C2704	0	*No damage*	0	*No damage*
C3140	0	*No damage*	0	*No damage*
AE 0.15	0	*No damage*	0.001	*Minimal damage*
C4611	0.15	*Minimal damage*	0.006	*Minimal damage*
C3115	0.37	*Minimal damage*	0.014	*Minimal damage*
C4624	0.71	*Generally repairable*	0.02	*Minimal damage*
AE 0.30	0.73	*Generally repairable*	0.041	*Minimal damage*
C4612	0.79	*Generally repairable*	0.037	*Minimal damage*
AE 0.50	Ult. (0.844)	***Significant damage***	0.091	*Minimal damage*
C3125	Ult. (0.844)	***Significant damage***	0.092	*Minimal damage*
C3135	Ult. (0.844)	***Significant damage***	0.083	*Minimal damage*
C4614	Ult. (0.844)	***Significant damage***	Ult. (0.552)	***Significant damage***

Ult: ultimate value.

Table 14
Max. and min. principal strains.

	Principal strain			
	First principal strain, ε_1 (x10^{-3})		Third principal strain, ε_3 (x10^{-3})	
C3301	<0.1	Allowable	0.18	Allowable
C0119	<0.1	Allowable	0.18	Allowable
C0120	<0.1	Allowable	0.20	Allowable
C2704	<0.1	Allowable	0.19	Allowable
C3140	<0.1	Allowable	0.21	Allowable
AE 0.15	<0.1	Allowable	0.18	Allowable
C4611	0.1	Allowable	0.24	Allowable
C3115	0.16	Allowable	0.31	Allowable
C4624	0.54	Allowable	0.37	Allowable
AE 0.30	0.75	Allowable	0.36	Allowable
C4612	0.89	Allowable	0.27	Allowable
AE 0.50	**1.93**	**Exceeded**	0.75	Allowable
C3125	**1.67**	**Exceeded**	0.62	Allowable
C3135	**1.90**	**Exceeded**	0.69	Allowable
C4614	**7.60**	**Exceeded**	1.32	Allowable

attributed to damage primarily occurring at the joints, specifically between the wall of the RCSB and the roof, as well as between the roof and the wall of the water tank.

The story drifts were obtained as the ratio of MRD to the wall distance from the ground floor. Among the analysis results, case C4614 indicated the highest value of 0.002 in the vertical direction at the P2 point. However, this result, along with the others, is within the allowable limits defined in Table 7.

For nonlinear analysis, another crucial safety limit is nonlinear hinge rotations. The magnitude of the rotational displacements in various cases is illustrated in Fig. 19. The case of C4614 exceeded the allowable limit for LS-C, which is 0.005 (as specified in Table 7). However, except for C4614, the nonlinear rotational deformations in the analyses exhibiting plastic deformation ranged from 0.0001 to 0.004 without exceeding the allowable limits. A detailed investigation of the results revealed that bending deformations were higher than torsional deformations. These tendencies were consistent with the modal shapes, particularly the first and second modes.

4.2. Plastic damage characteristics

Plastic damage refers to the irreversible deformations that occur in structural components when subjected to stresses beyond their elastic limits. The purpose of the analysis is to determine the degree of damage and the amount of plastic deformation. The results obtained from the analysis were compared to the values defined in Table 6, as shown in Table 13.

In tension, the results indicated that certain cases, such as C3301, C0119, C0120, C2704, and C3140, exhibited elastic behavior, meaning *no damage* occurred (see Table 13). *Minimal tension damage* was observed in the cases of C4611 and C3115 as shown in Fig. 20(b) and (c), requiring minor repairs. *Generally repairable tension damage* was noted in cases such as C4624, as shown in Fig. 20(d). As for *significant tension damage,* this phenomenon was observed in cases such as C3125, C3135, and C4614 where the maximum d_t reached to the ultimate value of 0.844, as indicated in Fig. 20(f), (g), and (j), respectively. In compression, only the C4614 earthquakes exhibited a maximum d_c of 0.552, corresponding to the ultimate value. Meanwhile, C3125 and C3135 resulted in *minimal compression damage*, as shown in Fig. 21. These results indicated that RCSB structure can be considered safe (within LS-D condition) under C3301, C0119, C0120, C2704, and C3140 earthquakes. In contrast, during C4614, C3125, and C3135 excitations the structure experienced large permanent distortions, falling short of collapse.

4.3. Strain states

The allowable first and third (maximum and minimum) principal strain limits (ε_1, ε_3), as described in Section 2.7, were employed as a guide for determining the degree of deformation and possible damage.

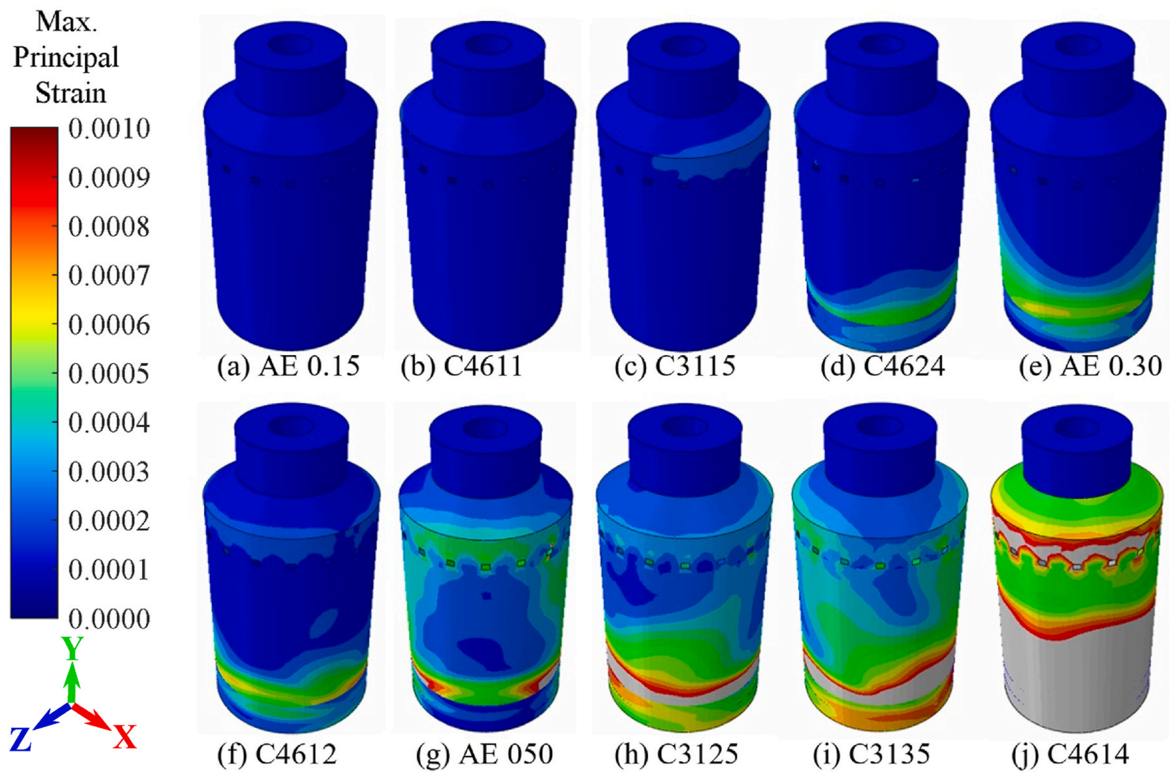

Fig. 22. Strain states.

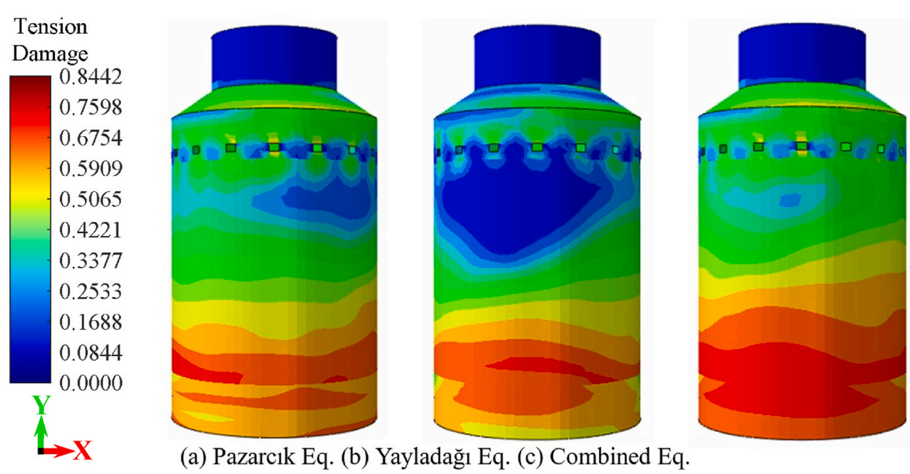

Fig. 23. Tension damage development of the mainshock-aftershock effect.

The results of the ε_1, ε_3 obtained from the different cases are shown in Table 14 and Fig. 22, along with a comparison to the allowable limits.

Notably, in the case of C4614, the results showed a much more significant exceedance compared to the other stations. Among the artificial earthquakes, only AE 0.50 exceeded the first principal strain limit. Meanwhile, the structure suffered significant damage during the cases of sequential earthquakes, specifically C3125, C3135, and C4614, as illustrated in Table 13 in Section 4.2. Also, the first principal strains due to consecutive earthquakes surpassed the allowable limits. However, the structural response remained within acceptable limits for the third principal strain even though the first principal strain in these cases exceeded the limit.

4.4. Mainshock-aftershock effects

In the analysis, two of the 12 cases showed remarkable differences due to sequential shocks, in which C3140 and C3125 were involved. Specifically, C3125 exhibited a damage development, while C3140 remained in the elastic range. In these cases, the change of structural responses was caused by the third earthquake (Yayladağı), which occurred on the same fault as the first earthquake (Pazarcık), rather than the second earthquake (Elbistan), which occurred in a nearby zone but on a different fault.

After analyzing the same model under singular earthquakes recorded by #3125 station, it was observed that the highest d_t was 0.81 under the first singular earthquake (Pazarcık), while the third singular earthquake (Yayladağı) had a maximum d_t of 0.77. Both values were below the ultimate value. However, the combined earthquake results reached an

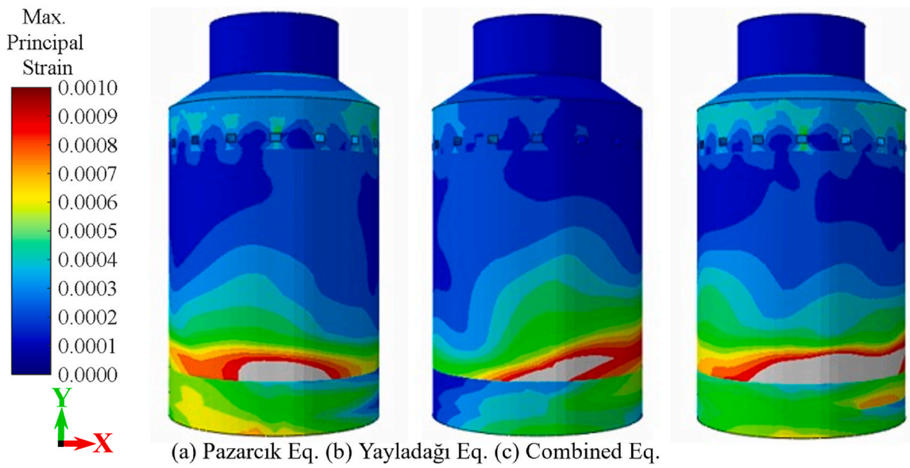

Fig. 24. Strain development due to the effect of the mainshock-aftershock effect.

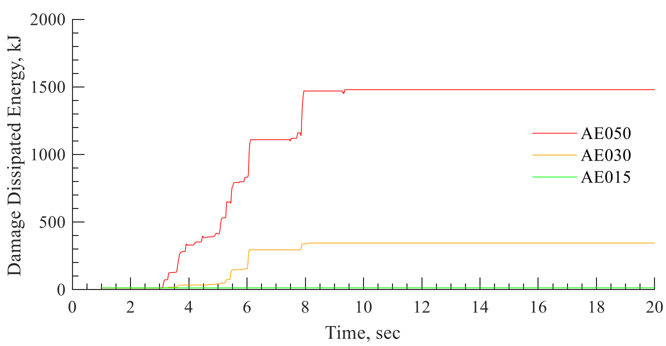

Fig. 25. Damage dissipated energy of the cases under AEs.

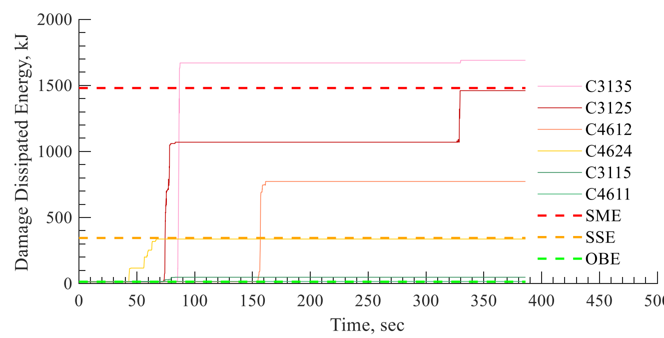

Fig. 26. Damage dissipated energy of the cases under combined earthquakes.

ultimate value of 0.8442, as shown in Fig. 23. Similarly, the d_c for the singular first and third earthquakes were 0.07 and 0.05, respectively, and it increased to 0.1 under the combined earthquake. Additionally, as shown in Fig. 24, although in three scenarios (two singular and one combined), the first principal strain reached the allowable limit, the extent of the affected zone increased due to the mainshock-aftershock effect.

The findings also indicated that the PFAs and MRDs at various points of the RCSB exhibited differences between the results of singular earthquakes and combined earthquakes for the case of C3125. For instance, at the top floor of the RCSB building, the MRDs in the Z direction were 63.93 mm and 71.92 mm under the singular Pazarcık and Yayladağı earthquakes, respectively, whereas the MRD increased to 74.19 mm under combined conditions. Additionally, similar to these findings, the case of C3140 also exhibited different results for PFAs and MRDs under singular and combined earthquakes; however, it did not experience plastic deformation.

4.5. Energy state

Damage dissipated energy refers to the energy absorbed and converted into permanent deformation within a material when subjected to stress beyond its elastic limit. Fig. 25 shows the cumulative energy dissipated over time of the three artificial earthquakes. Among that, the AE 0.15 case showed insignificant dissipated energy, indicating that the material mainly remained within its elastic limit during this event. The AE 0.30 case exhibited a dissipated energy of approximately 345 kJ, reflecting a moderate level of permanent deformation. However, the AE 0.50 case showed a much higher dissipated energy, reaching around 1482 kJ, which was approximately 4.3 times greater than the AE 0.30 case. Again, it should be noted that AE 0.15, AE 0.30, and AE 0.50 were considered as the OBE, SSE, and SME levels, respectively.

The most noticeable result was from the C4614 condition, which demonstrated an exceptionally high dissipated energy of 14,800 kJ. This value was approximately ten times higher than the SME level and 43 times higher than the SSE level. Fig. 26, excluding the result of C4614 for clarity, effectively illustrates the damage dissipation energy for the remaining conditions. The C3135 case exhibited around 1690 kJ of dissipated energy, surpassing the SME level. Similarly, the C3125 case had a value quite close to the SME level. The case of C4624 had dissipated energy similar to the SSE level, while the C4612 case showed more than double this amount but less than the SME level. The cases of C4611 and C3115 displayed only negligible dissipated energy, with values of 16.0 kJ and 47.7 kJ, respectively, indicating minimal damage under the given conditions. Additionally, the other cases, including C0119, C0120, C3301, C3140, and C2704, revealed no damage dissipated energy. Moreover, after the Yayladağı earthquake occurred, the dissipated energy increased in some cases. For instance, a significant increase was observed in the case of C3125, where the dissipated energy rose from 1073 kJ to 1464 kJ, implying the mainshock-aftershock effect.

Table 15 summarizes the analysis results of RCSB of the AP1000 NPPs subjected to 12 different earthquake cases in comparison with the corresponding allowable limits. The table provides the maximum PGA among the X, Y, and Z directions instead of illustrating all directions. The results of PFA, MRD, tension and compression damage, and damage dissipated energy from the cases under actual combined earthquakes were compared to the LSs obtained from AEs (in Table 6). It should be noted that the allowable drift ratio and nonlinear hinge rotations were described in Section 2.7 according to ASCE 43-5 ("ASCE/SEI 43, 2005), and the allowable principal strains were also explained in Section 2.7.

Table 15
Comparison results with limit states.

Cases	*PGA, g	PFA, g	MRD, mm	Drift ratio, γ_a	NL. hinge rotation, θ_A	First principal strain, ε_1	Third principal strain, ε_3	Tens. damage	Comp. damage	Damage dissipated energy
C3301	0.05	LS-C	LS-C	LS-D	LS-C	Allow.	Allow.	LS-C	LS-C	LS-C
C0119	0.05	LS-C	LS-C	LS-D	LS-C	Allow.	Allow.	LS-C	LS-C	LS-C
C0120	0.12	LS-C	LS-C	LS-D	LS-C	Allow.	Allow.	LS-C	LS-C	LS-C
C2704	0.16	LS-C	LS-C	LS-D	LS-C	Allow.	Allow.	LS-C	LS-C	LS-C
C3140	0.22	LS-B	LS-B	LS-D	LS-C	Allow.	Allow.	LS-C	LS-B	LS-B
C3115	0.29	LS-B	LS-B	LS-D	LS-C	Allow.	Allow.	LS-B	LS-B	LS-B
C4611	0.36	LS-B	LS-B	LS-D	LS-C	Allow.	Allow.	LS-B	LS-B	LS-B
C4624	0.36	LS-A	LS-A	LS-D	LS-C	Allow.	Allow.	LS-A	LS-B	LS-B
C4612	**0.65**	LS-A	LS-A	LS-D	LS-C	Allow.	Allow.	LS-A	LS-B	LS-A
C3125	**1.17**	**Exc.**	**Exc.**	LS-D	LS-C	**Exc.**	Allow.	**Sign.**	LS-B	LS-A
C3135	**1.40**	**Exc.**	**Exc.**	LS-D	LS-C	**Exc.**	Allow.	**Sign.**	LS-B	**Exc.**
C4614	**2.22**	**Exc.**	**Exc.**	LS-D	**Exc.**	**Exc.**	Allow.	**Sign.**	**Sign.**	**Exc.**

(*PGA presents the value of the direction where the value is higher., Allow.: allowable value Exc.: exceeded, Sign.: significant damaged, NL.: nonlinear.).

5. Conclusions

In this study, 12 cases consisting of three earthquake sequences that occurred in Türkiye in 2023 within a short time frame were used to evaluate the seismic vulnerability of the RCSB of the AP1000 NPPs. For this purpose, a series of numerical analyses were conducted to evaluate the structural dynamic responses, damage characteristics, strain states, and damage dissipated energies of the model under those conditions. The comparative analysis of the RCSB also highlighted the effects of mainshock-aftershock sequences. The following conclusions can be drawn.

(1) The Pazarcık station (#4614) record causes significant damage to the RCSB structure. All structural responses, including PFA, MRD, principal stress, and strain values, exceed the LSs.
(2) In other cases, some stations (#3125, #3135) located in Hatay Province also indicate severe results. In these cases, tensional damage to the structure was generally observed. Although the maximum principal strain and damage parameters exceeded the allowable levels, none of the cases exceeded the allowable drift ratio or nonlinear hinge rotation.
(3) The structural responses due to some stations in Kahramanmaraş and Hatay Provinces (#4612, #4624, #4611, and #3115) are comparable to those under the SSE level or higher than the OBE level in most analyses.
(4) The cases consisting of the records from certain stations in Adana, Mersin, and Gaziantep Provinces (#0119, #0120, #3301, and #2704) exhibit elastic behavior and without structural damages.
(5) The mainshock-aftershock affects dynamic responses, damage statements, strain, and damage dissipated energies of RCSB significantly. Therefore, it is necessary to consider the influence of mainshock-aftershock in seismic analyses and designs of NPP structures.

CRediT authorship contribution statement

Tandogan Mesut: Writing – original draft, Investigation, Formal analysis. **Duy-Duan Nguyen:** Writing – review & editing, Validation. **Duy-Liem Nguyen:** Writing – original draft, Data curation. **Duc-Kien Thai:** Writing – review & editing, Supervision, Conceptualization.

Declaration of competing interest

The authors declare that they have no known competing financial interests or personal relationships that could have appeared to influence the work reported in this paper.

Data availability

No data was used for the research described in the article.

References

Abdelnaby, A., Elnashai, A., 2015. Numerical modeling and analysis of RC frames subjected to multiple earthquakes. Earthquakes and Structures 9, 957–981.
Bathe, K.J., 1996. Finite Element Procedures. Upper Saddle River, New Jersey.
Chen, W., Zhang, Y., Wang, D., 2021. Damage development analysis of the whole nuclear power plant of AP1000 type under strong Main-aftershock sequences. Nucl. Eng. Des. 371, 110975.
Chopra, A.K., 1995. Dynamics of Structures: Theory and Applications to Earthquake Engineering. Prentice Hall, Englewood Cliffs, New Jersey.
Cui, Z.-D., Sui, T.-Y., Wang, S.-Y., Yuan, L., 2024. Seismic response of subway station subjected to mainshock-aftershock sequences by centrifuge shaking table tests. Soil Dynam. Earthq. Eng. 176, 108327.
Fakharifar, M., Chen, G., Sneed, L., Dalvand, A., 2015. Seismic performance of post-mainshock FRP/steel repaired RC bridge columns subjected to aftershocks. Compos. B Eng. 72, 183–198.
Hatzigeorgiou, G.D., Beskos, D.E., 2009. Inelastic displacement ratios for SDOF structures subjected to repeated earthquakes. Eng. Struct. 31 (11), 2744–2755.
Jiang, X., Song, X., Li, T., Wu, K., 2023. Moment magnitudes of two large Turkish earthquakes on February 6, 2023 from long-period coda. Earthq. Sci. 36 (2), 169–174.
Kennedy, R.P., 1985. Various Types of Reported Seismic Margins and Their Uses. United States.
Li, Q., Zhang, J., 2013. Preliminary research on the elimination of OBE in the seismic design of NPP. In: Volume 3: Nuclear Safety and Security; Codes, Standards, Licensing and Regulatory Issues; Computational Fluid Dynamics and Coupled Codes, Chengdu, China, V003T07A001.
Lin, F., Li, H., 2017. Safety analysis of nuclear containment vessels subjected to strong earthquakes and subsequent tsunamis. Nucl. Eng. Technol. 49 (5), 1079–1089.
Lo Frano, R., Forasassi, G., 2012. Preliminary evaluation of structural response of ELSY reactor in the after shutdown condition. Nucl. Eng. Des. 246, 298–305.
Lubliner, J., Oliver, J., Oller, S., Oñate, E., 1989. A plastic-damage model for concrete. Int. J. Solid Struct. 25 (3), 299–326.
Methodologies for Seismic Safety Evaluation of Existing Nuclear Installations, 2020. International Atomic Energy Agency (IAEA), Vienna, Avusturia.
Moon, J., Roeder, C.W., Lehman, D.E., Lee, H.-E., 2012. Analytical modeling of bending of circular concrete-filled steel tubes. Eng. Struct. 42, 349–361.
Murphy, A.J., Tegeler, B.A., 2007. Evaluation of the Seismic Design Criteria in ASCE/SEI Standard 43-05 for Application to Nuclear Power Plants. U.S. Nuclear Regulatory Commission (NRC), Washington, DC.
Newmark, N.M., Hall, W.J., 1991. NUREG-1407: Procedural and Submittal Guidance for the Individual Plant Examination of External Events (IPEEE) for Severe Accident Vulnerabilities. U.S. Nuclear Regulatory Commission (NRC), Washington, D.C., USA, Jun-.
Pang, R., Zai, D., Xu, B., Liu, J., Zhao, C., Fan, Q., Chen, Y., 2023a. Stochastic dynamic and reliability analysis of AP1000 nuclear power plants via DPIM subjected to mainshock-aftershock sequences. Reliab. Eng. Syst. Saf. 235, 109217.
Pang, R., Zai, D., Xu, B., Liu, J., Zhao, C., Fan, Q., Chen, Y., 2023b. Stochastic dynamic and reliability analysis of AP1000 nuclear power plants via DPIM subjected to mainshock-aftershock sequences. Reliab. Eng. Syst. Saf. 235, 109217.
Probabilistic Safety Assessment for Seismic Events, 2020. International Atomic Energy Agency (IAEA), Vienna, Avusturia.
Seismic Hazard Evaluations for, U.S., 2021. Nuclear Power Plants: Near-Term Task Force Recommendation 2.1 Results. U.S. Nuclear Regulatory Commission (NRC), Washington, D.C., USA.
Seismic Safety and Regulatory Activitie, 2024. Nuclear Safety and Security Commission (NSSC). Seoul, South Korea.

Stramandinoli, R., Rovere, H., 2008. An efficient tension-stiffening model for nonlinear analysis of reinforced concrete members. Eng. Struct. 30, 2069–2080.
Wang, D., Wu, C., Zhang, Y., Ding, Z., Chen, W., 2019. Elastic-plastic behavior of AP1000 nuclear island structure under mainshock-aftershock sequences. Ann. Nucl. Energy 123, 1–17.
Wight, J.K., MacGregor, J.G., 2011. In: Reinforced Concrete: Mechanics and Design, sixth ed. Pearson Prentice Hall, New Jersey.
Xie, W.-C., Ni, S.-H., Liu, W., Jiang, W., 2019. In: Seismic Risk Analysis of Nuclear Power Plants, first ed. Cambridge University Press.
Yip, W.K., 1998. Generic form of stress-strain equations for concrete. Cement Concr. Res. 28 (4), 499–508.
Yu, N., Zhao, C., Peng, T., Huang, H., Roy, S.S., Mo, Y.L., 2019. Numerical investigation of AP1000 NIB under mainshock-aftershock earthquakes. Prog. Nucl. Energy 117, 103096.
Zengin, B., Aydin, F., 2023. The effect of material quality on buildings moderately and heavily damaged by the Kahramanmaraş earthquakes. Appl. Sci. 13 (19), 10668.
Zhai, C.-H., Zheng, Z., Li, S., Xie, L.-L., 2015. Seismic analyses of a RCC building under mainshock–aftershock seismic sequences. Soil Dynam. Earthq. Eng. 74, 46–55.
Zhai, C.-H., Zheng, Z., Li, S., Pan, X., 2017. Damage accumulation of a base-isolated RCC building under mainshock-aftershock seismic sequences. KSCE J. Civ. Eng. 21 (1), 364–377.
Zhai, C.-H., Bao, X., Zheng, Z., Wang, X.-Y., 2018. Impact of aftershocks on a post-mainshock damaged containment structure considering duration. Soil Dynam. Earthq. Eng. 115, 129–141.
Zhang, M., 1997. Study on similitude laws for shaking table tests. Earthq. Eng. Eng. Vib. 17 (2), 52–58.
Zhang, S., Wang, G., Sa, W., 2013. Damage evaluation of concrete gravity dams under mainshock–aftershock seismic sequences. Soil Dynam. Earthq. Eng. 50, 16–27.
Zhang, X., Zhao, C., Zhi, L., Pang, R., Mo, Y.L., 2024. Seismic fragility analysis of shield building considering strength ratio of mainshock and aftershocks. Nucl. Eng. Technol. 56 (8), 3397–3404.
Zhao, C., Yu, N., Peng, T., Gautam, A., Mo, Y.L., 2020a. Vulnerability assessment of AP1000 NPP under mainshock-aftershock sequences. Eng. Struct. 208, 110348.
Zhao, C., Yu, N., Peng, T., Lippolis, V., Corona, A., Mo, Y.L., 2020b. Study on the dynamic behavior of isolated AP1000 NIB under mainshock-aftershock sequences. Prog. Nucl. Energy 119, 103144.
Zhao, J., Chen, H., Zhou, Z., 2023. Shaking table test study of nuclear power plant model considering soil-structure interaction effect. Soil Dynam. Earthq. Eng. 168, 107859.
ABAQUS/CAE User's Guide," Simulia.
ACI 349-01: Code Requirements for Nuclear Safety Related Concrete Structures, 2001. American Concrete Institute (ACI), Farmington Hills, MI, USA.
ASCE/SEI 4-16: Seismic Analysis of Safety-Related Nuclear Structures, 2017. American Society of Civil Engineers (ASCE), Reston, VA, USA.
ASCE/SEI 43-05: Seismic Design Criteria for Structures, Systems, and Components in Nuclear Facilities, 2005. American Society of Civil Engineers (ASCE), Reston, VA, USA.
CEB-FIP Model Code 2010, Part II, Section 5.1, 2010. Committee Euro-International du Beton.
RG 1.61: Damping Values for Seismic Design of Nuclear Power Plants, 2007. U.S. Nuclear Regulatory Commission (NRC), Washington, D.C., USA.
RG 1.60: Design Response Spectra for Seismic Design of Nuclear Power Plants, 2014. U.S. Nuclear Regulatory Commission (NRC), Washington, D.C., USA.